



### **Science Arts & Métiers (SAM)**

is an open access repository that collects the work of Arts et Métiers Institute of Technology researchers and makes it freely available over the web where possible.

This is an author-deposited version published in: <https://sam.ensam.eu>  
Handle ID: <http://hdl.handle.net/10985/24324>



This document is available under CC BY license

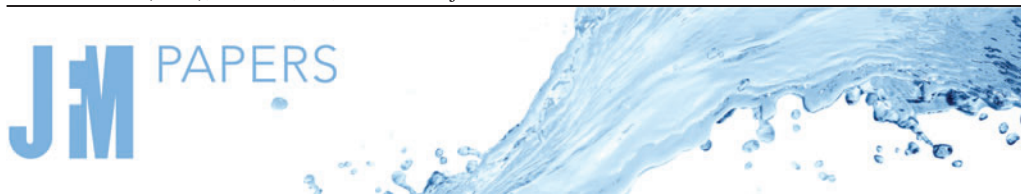
#### **To cite this version :**

Mario STOJANOVI, Francesco ROMANO, Hendrik C. KUHLMANN - Stability of thermocapillary flow in liquid bridges fully coupled to the gas phase - Journal of Fluid Mechanics - Vol. 949, - 2022

Any correspondence concerning this service should be sent to the repository

Administrator : [scienceouverte@ensam.eu](mailto:scienceouverte@ensam.eu)





# Stability of thermocapillary flow in liquid bridges fully coupled to the gas phase

Mario Stojanović<sup>1,†</sup>, Francesco Romano<sup>2,†</sup> and Hendrik C. Kuhlmann<sup>1,†</sup>

<sup>1</sup>TU Wien, Getreidemarkt 9-BA, 1060 Vienna, Austria

<sup>2</sup>Univ. Lille, CNRS, ONERA, Arts et Métiers Institute of Technology, Centrale Lille, UMR 9014 – LMFL – Laboratoire de Mécanique des Fluides de Lille – Kampé de Fériet, F-59000 Lille, France

(Received 9 April 2022; revised 7 July 2022; accepted 5 August 2022)

The linear stability of the axisymmetric steady thermocapillary flow in a liquid bridge made from 2cSt silicone oil (Prandtl number 28) is investigated numerically in the framework of the Boussinesq approximation. The flow and temperature fields in the surrounding gas phase (air) are taken into account for a generic cylindrical container hosting the liquid bridge. The flows in the liquid and in the gas are fully coupled across the hydrostatically deformed liquid–gas interface, neglecting dynamic interface deformations. Originating from a common reference case, the linear stability boundary is computed varying the length of the liquid bridge (aspect ratio), its volume and the gravity level, providing accurate critical data. The qualitative dependence of the critical threshold on these parameters is explained in terms of the characteristics of the critical mode. The heat exchange between the ambient gas and the liquid bridge that is fully resolved has an important influence on the critical conditions.

**Key words:** thermocapillarity, instability, liquid bridge, gas/liquid flow

## 1. Introduction

The interfacial free energy between two immiscible fluids depends on the local temperature. If the temperature varies along the interface, then the associated energy gradients lead to variations of the line tension. This is the thermocapillary effect (Thomson 1855; Scriven & Sternling 1960; Levich & Krylov 1969), which can be a major driving force for fluid motion in pure fluids. Thermocapillary flows are of great importance for industrial applications such as welding (Mills *et al.* 1998), combustion (Sirignano &

† Email addresses for correspondence: [mario.stojanovic@tuwien.ac.at](mailto:mario.stojanovic@tuwien.ac.at), [francesco.romano@ensam.eu](mailto:francesco.romano@ensam.eu), [hendrik.kuhlmann@tuwien.ac.at](mailto:hendrik.kuhlmann@tuwien.ac.at)

Glassman 1970), crystal growth (Schwabe 1981) and droplet manipulation in microfluidics (Young, Goldstein & Block 1959).

To better understand thermocapillary flows, a number of paradigmatic configurations have been investigated, ranging from flows in thin films (Smith & Davis 1983*a, b*; Oron, Davis & Bankoff 1997; Diez & Kondic 2002; Craster & Matar 2009), flows in liquid-filled cavities with a non-isothermal interface (Carpenter & Homsy 1989; Ohnishi, Azuma & Doi 1992; Xu & Zebib 1998; Kuhlmann & Albensoeder 2008; Romanò & Kuhlmann 2017), and axisymmetric liquid bridges kept in place by the mean surface tension and aligned with the gravity vector (Chun & Wuest 1979; Preisser, Schwabe & Scharmann 1983; Kuhlmann 1999; Kawamura & Ueno 2006; Schwabe 2014; Kumar 2015; Romanò & Kuhlmann 2018). The canonical system of a liquid bridge is often employed to model the fundamental transport processes in the floating-zone technique of crystal growth (Pfann 1962; Hurlé & Jakeman 1981). A major aspect in floating-zone crystal growth is the onset of time-dependent melt flow, because it is associated with a time-dependent propagation of the solidification front, which leads to an uneven distribution of impurities (striations) in the desired single crystal (Cröll *et al.* 1991).

In the floating-zone technique, the liquid bridge is supported by solid crystalline or polycrystalline rods whose temperature near the melt zone is close to the melting point, while the temperature of the interface, which is heated, exhibits a maximum midway between the two supports. To simplify the problem while retaining the essential flow physics, the half-zone model has been introduced by Schwabe *et al.* (1978). In their half-zone model, two support rods of a material with a higher melting point than the liquid are used and kept at different temperatures. The strength of the flow in the half-zone depends on the applied temperature difference, often measured by a suitable Reynolds number  $Re$ . As the Reynolds number is increased, the axisymmetric steady flow in the half-zone becomes unstable. As these flow instabilities are related to the striations found in crystals produced by the floating-zone technique, much effort has been devoted to flow instabilities in the half-zone model (Kuhlmann 1999), which led to numerous experimental (Preisser *et al.* 1983; Velten, Schwabe & Scharmann 1991; Takagi *et al.* 2001; Ueno, Tanaka & Kawamura 2003; Kawamura & Ueno 2006; Gaponenko, Mialdun & Shevtsova 2012; Yano *et al.* 2017; Kang *et al.* 2019) and numerical (Wanschura *et al.* 1995; Leypoldt, Kuhlmann & Rath 2000; Levenstam, Amberg & Winkler 2001; Lappa, Savino & Monti 2001; Nienhüser & Kuhlmann 2002; Shevtsova, Gaponenko & Nepomnyashchy 2013; Li *et al.* 2015; Motegi, Fujimura & Ueno 2017*a*) investigations, only a few of which can be cited here. Investigations of the full-zone problem are sparse (see, however, Wanschura, Kuhlmann & Rath 1997*a*; Kasperski, Batoul & Labrosse 2000; Lappa 2003, 2004, 2005; Hu, Tang & Li 2008; Motegi, Kudo & Ueno 2017*b*).

The stability of the flow in a thermocapillary liquid bridge is a complex problem, because the flow and temperature fields in the gas and the liquid phase are coupled via a deformable interface. For this reason, most of the theoretical and numerical studies have made simplifying assumptions. The most popular approximation is to consider the interface indeformable (Shevtsova & Legros 1998; Nienhüser & Kuhlmann 2002) or even cylindrical (see e.g. Neitzel *et al.* 1993; Wanschura *et al.* 1995). Furthermore, the ambient atmosphere is often considered a passive gas that does not exert any viscous stresses on the interface and which may even be considered adiabatic. In this way, the two-phase problem is approximated by a single-phase problem that depends on only a few non-dimensional parameters. Within the single-fluid model, the dependence on the Prandtl number of the critical Reynolds number at which the instability arises has been established numerically by Wanschura *et al.* (1995) and Levenstam *et al.* (2001): for large Prandtl

numbers ( $Pr \gtrsim 1$ ), the axisymmetric flow becomes unstable to hydrothermal waves upon increasing the Reynolds number, while the first instability at low Prandtl numbers ( $Pr \lesssim 1$ ) is three-dimensional but steady.

The stationary three-dimensional instability was discovered by Levenstam & Amberg (1994, 1995) using numerical simulation, and by Wanschura *et al.* (1995) using linear stability analysis. The instability has been compared with the instability of vortex rings, and its mechanics was further detailed by Wanschura *et al.* (1995) who noted that the instability is purely inertial, while the temperature field serves only to drive the basic flow. Leypoldt, Kuhlmann & Rath (2002) carried out numerical simulations and explained the second instability at low Prandtl numbers when the steady three-dimensional flow becomes time-dependent. The second critical Reynolds number was further investigated by Motegi *et al.* (2017a) using a numerical Floquet stability analysis. Further investigation of the low-Prandtl-number instabilities are due to Takagi *et al.* (2001), Imaishi *et al.* (2001), Li *et al.* (2007, 2008) and Fujimura (2013).

For high Prandtl numbers, Wanschura *et al.* (1995) identified numerically the critical mode as a hydrothermal wave, a concept first introduced by Smith & Davis (1983a). Hydrothermal waves are characterised by locally strong temperature extrema in the bulk while the thermal wave is very weak on the interface. At the onset, a weak perturbation flow is driven primarily by azimuthal temperature gradients (thermocapillary stresses). The associated return flow transports basic state temperature in the bulk, which leads to the large internal perturbation temperature extrema that feed back on the free surface. Preisser *et al.* (1983) found experimentally the approximate correlation  $m \approx 2.2/\Gamma$  for the dependence of the critical wavenumber  $m$  on the length-to-radius aspect ratio  $\Gamma = d/R$  at the onset of oscillations. This dependence was confirmed within the linear stability analysis of Wanschura *et al.* (1995) and others. However, the results of Wanschura *et al.* (1995) were obtained for moderate Prandtl numbers, zero gravity and an indeformable adiabatic free surface. Therefore, they deviate from the extensive measurements of Velten *et al.* (1991), indicating that much finer and more realistic modelling is necessary.

The effect of the shape (slender/fat) of high-Prandtl-number liquid bridges on the critical Reynolds number has been investigated experimentally by Hu *et al.* (1994), Masud, Kamotani & Ostrach (1997) and Sakurai, Ohishi & Hirata (2004). Shevtsova & Legros (1998) carried out numerical simulations. Using the assumption of an adiabatic free surface, Nienhüser & Kuhlmann (2002) and Nienhüser (2002) calculated numerically the impact of the static shape of the liquid bridge and of buoyancy forces on the linear stability of an axisymmetric flow. Their study overcame the limits of stability analyses, which were restricted before to cylindrical bridges. For volumes of liquid of approximately 90 % of the straight cylindrical volume, the high-Prandtl-number axisymmetric steady flow is remarkably stable (see e.g. Sakurai, Ohishi & Hirata 1996; Chen & Hu 1998).

Even though Fu & Ostrach (1985) computed rudimentarily a coupled liquid–gas flow, early numerical attempts to model the heat transfer across the interface were typically based on Newton’s law of heat transfer (see e.g. Shen 1989; Neitzel *et al.* 1993; Nienhüser & Kuhlmann 2001; Fujimoto *et al.* 2019; Carrión, Herrada & Montanero 2020). A recent study by Romanò & Kuhlmann (2019) has shown, however, that modelling the heat transfer across the interface by Newton’s law tends to underestimate the thermocapillary driving, except very close to the cold rod. Motivated by the experimental evidence of the strong impact of the heat transfer across the interface (Kamotani *et al.* 2003; Yano *et al.* 2017), and with improved computing capabilities, more recent numerical approaches take into account the flow and heat transport in the surrounding gas phase (Shevtsova *et al.* 2014; Watanabe *et al.* 2014). Also, the possibility of imposing an external gas flow shows

promise for a control of the onset of hydrothermal waves. This perspective stimulated new experiments (Ueno, Kawazoe & Enomoto 2010; Irikura *et al.* 2005; Gaponenko *et al.* 2021) and numerical investigations (Yasnou *et al.* 2018) with imposed axial gas flow.

The present work is aimed at a linear stability analysis of the flow in a thermocapillary liquid bridge including the gas phase. To that end, we use our linear stability code MaranStable, which has been significantly extended and improved since its earlier version (see e.g. Shevtsova *et al.* 2014). Owing to the large parameter space, a liquid bridge made of 2cSt silicone oil is considered ( $Pr = 28$ ), which has often been employed in experiments (Yano *et al.* 2018c), fully coupled to the surrounding air. The material parameters are assumed constant, and the interface is indeformable. Stability analyses are carried out quasi-continuously varying the aspect ratio, the volume fraction and the gravity level. The relevance of such data is understood when considering that accurate numerical studies in such high-Prandtl-number liquid bridges are hardly reported in the literature, even though they are of great interest for experiments on stability and particle accumulation studies on the ground and under zero gravity. On the ground buoyancy-driven flow is always coupled to and interferes with a thermocapillary flow. Under zero gravity, however, buoyancy can be eliminated. This property is utilised in space experiments like MEIS (Kawamura *et al.* 2012), Dynamic Surf (Yano *et al.* 2018b) and JEREMI (planned; Barmak, Romanò & Kuhlmann 2021).

To compute the linear stability of the axisymmetric flow and its dependence on the parameters, we first formulate the governing equations and boundary conditions in § 2. Thereafter, in § 3 the linear stability approach and the post-processing are described. The results are presented and discussed in § 4, interpreting the stability boundaries in the light of the multi-phase energy budgets. We close with a discussion and conclusions in § 5.

## 2. Problem formulation

### 2.1. The setup

We consider an axisymmetric liquid bridge of a Newtonian liquid captured between two coaxial cylindrical rods both of length  $d_{rod}$ . The liquid bridge has axial length  $d$  and is assumed to be pinned to the sharp circular edges of the rods of radius  $r_i$ , as shown in figure 1. The rods are aligned parallel to the acceleration of gravity  $\mathbf{g} = -g\mathbf{e}_z$ , where  $\mathbf{e}_z$  is the axial unit vector, and mounted coaxially in a closed cylindrical chamber of radius  $r_o > r_i$  and height  $2d_{rod} + d$  filled with a gas. We use cylindrical coordinates  $(r, \varphi, z)$  centred in the middle of the liquid bridge, and corresponding unit vectors  $(\mathbf{e}_r, \mathbf{e}_\varphi, \mathbf{e}_z)$  such that the position vector is  $\mathbf{x} = r\mathbf{e}_r + z\mathbf{e}_z$ , and the velocity field is represented by  $\mathbf{u} = u\mathbf{e}_r + v\mathbf{e}_\varphi + w\mathbf{e}_z$ . The characteristic geometrical parameters are

$$\Gamma = \frac{d}{r_i}, \quad \Gamma_{rod} = \frac{d_{rod}}{r_i}, \quad \eta = \frac{r_o}{r_i}, \quad (2.1a-c)$$

where  $\Gamma$  and  $\Gamma_{rod}$  are the aspect ratio of the liquid bridge and of the rods, respectively, and  $\eta$  is the radius ratio of the chamber.

While the cylindrical sidewall and the annular top and bottom walls of the chamber are assumed to be adiabatic, the cylindrical support rods are kept at different but constant temperatures  $T_{hot} = T_0 + \Delta T/2$  and  $T_{cold} = T_0 - \Delta T/2$ , respectively, where  $T_0 = (T_{hot} + T_{cold})/2$  is the mean temperature, hereinafter used as the reference temperature. The enforced temperature variation across the liquid bridge creates a variation of the

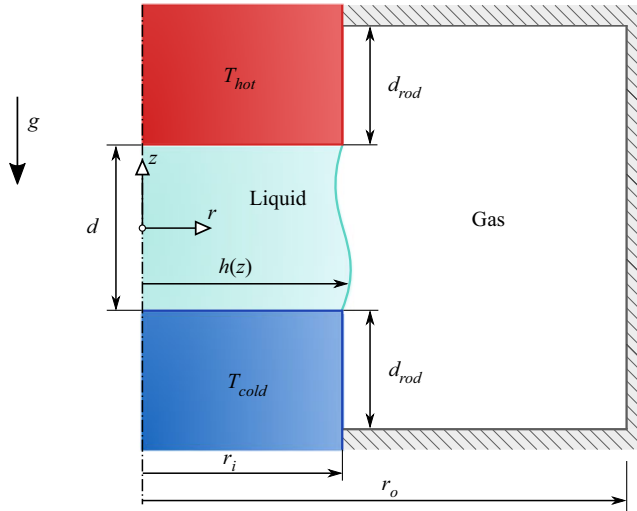


Figure 1. Schematic of the problem set-up and coordinates. The hot (red) and cold (blue) solid rods supporting the liquid bridge (light blue) are mounted coaxially in a closed cylindrical gas container (grey, hatched). Gravity acts in the negative  $z$  direction and leads to the hydrostatic shape  $h(z)$  of the liquid bridge. The system is axisymmetric with respect to the dash-dotted line ( $r = 0$ ).

surface tension that can be described, to first order, by the linear dependence

$$\sigma(T) = \sigma_0 - \gamma(T - T_0) + O[(T - T_0)^2], \quad (2.2)$$

where  $\sigma_0 = \sigma(T_0)$  is the surface tension at the mean temperature, and  $\gamma = -\partial\sigma/\partial T|_{T=T_0}$  is the negative surface tension coefficient. The resulting surface tension gradients induce tangential shear stresses via the thermocapillary effect, which lead to an axisymmetric thermocapillary flow on both sides of the interface (Kuhlmann 1999).

In addition to the thermocapillary stresses, the flow in the liquid is driven by buoyancy forces due to the temperature dependence of the density of the liquid:

$$\rho(T) = \rho_0\{1 - \beta(T - T_0) + O[(T - T_0)^2]\}, \quad (2.3)$$

where  $\rho_0 = \rho(T_0)$  is the liquid density at the reference temperature, and  $\beta = -\rho_0^{-1}(\partial\rho/\partial T)_p$  is the thermal expansion coefficient. Buoyancy forces also act in the gas phase due to the temperature-induced density variation of the gas in contact with the liquid–gas interface. For short liquid bridges employed in terrestrial laboratories, thermocapillary surface forces typically dominate over buoyant volume forces.

## 2.2. Governing equations

To compute the axisymmetric flow and temperature fields, and to investigate the hydrodynamic stability of the flow, the governing transport equations must be solved subject to the respective boundary conditions.

### 2.2.1. Transport equations

To non-dimensionalise the governing equations, we adopt the thermocapillary diffusive scaling given in table 1 (see e.g. Kuhlmann 1999), where  $\nu$  is the constant kinematic viscosity of the liquid at the reference temperature. The temperature dependence of the



---

Variable	$\mathbf{x}$	$t$	$\mathbf{u}$	$p$	$T$
Scale	$d$	$d^2/\nu$	$\gamma \Delta T/\rho_0 \nu$	$\gamma \Delta T/d$	$\Delta T$

---

Table 1. Scaling.

density in the liquid and in the gas is taken into account within the Oberbeck–Boussinesq approximation (Landau & Lifschitz 1959; Mihaljan 1962). In this formulation, the Navier–Stokes, continuity and energy equations for the liquid phase read

$$\frac{\partial \mathbf{u}}{\partial t} + Re \mathbf{u} \cdot \nabla \mathbf{u} = -\nabla p + \nabla^2 \mathbf{u} + Bd \vartheta \mathbf{e}_z, \quad (2.4a)$$

$$\nabla \cdot \mathbf{u} = 0, \quad (2.4b)$$

$$\frac{\partial \vartheta}{\partial t} + Re \mathbf{u} \cdot \nabla \vartheta = \frac{1}{Pr} \nabla^2 \vartheta, \quad (2.4c)$$

where  $\vartheta = (T - T_0)/\Delta T$  is the normalised deviation from the reference temperature. The fluid motion depends on the thermocapillary Reynolds, Prandtl and dynamic Bond numbers defined as

$$Re = \frac{\gamma \Delta T d}{\rho_0 \nu^2}, \quad Pr = \frac{\nu}{\kappa}, \quad Bd = \frac{\rho_0 g \beta d^2}{\gamma}, \quad (2.5a-c)$$

where  $\kappa$  is the constant thermal diffusivity of the liquid at the reference temperature. Instead of  $Re$ , the Marangoni number  $Ma = Re Pr$  can be used.

Using the same scaling, the flow in the gas phase is governed by

$$\frac{\partial \mathbf{u}_g}{\partial t} + Re \mathbf{u}_g \cdot \nabla \mathbf{u}_g = -\frac{1}{\tilde{\rho}} \nabla p_g + \tilde{\nu} \nabla^2 \mathbf{u}_g + \tilde{\beta} Bd \vartheta_g \mathbf{e}_z, \quad (2.6a)$$

$$\nabla \cdot \mathbf{u}_g = 0, \quad (2.6b)$$

$$\frac{\partial \vartheta_g}{\partial t} + Re \mathbf{u}_g \cdot \nabla \vartheta_g = \frac{\tilde{\kappa}}{Pr} \nabla^2 \vartheta_g, \quad (2.6c)$$

where the non-dimensional field quantities are indicated by the subscript  $g$ . The additional non-dimensional parameters are the gas-to-liquid ratios of the density  $\tilde{\rho} = \rho_g/\rho_0$ , the kinematic viscosity  $\tilde{\nu} = \nu_g/\nu$ , the thermal diffusivity  $\tilde{\kappa} = \kappa_g/\kappa$ , and the thermal expansion coefficient  $\tilde{\beta} = \beta_g/\beta$ . Introducing

$$\boldsymbol{\alpha} = (\alpha_\rho, \alpha_\nu, \alpha_\kappa, \alpha_\beta) = \begin{cases} (1, 1, 1, 1), & \text{for the liquid phase,} \\ (\tilde{\rho}, \tilde{\nu}, \tilde{\kappa}, \tilde{\beta}), & \text{for the gas phase,} \end{cases} \quad (2.7)$$

allows us to refer to both phases at the same time, while keeping the notation succinct.

### 2.2.2. Boundary conditions

(i) Support rods. To be able to control experimentally the temperatures imposed on the liquid bridge, the heating rods are typically made from good thermal conductors.

Accordingly, the surfaces of the rods are modelled as isothermal, no-slip and no-penetration walls,

$$\text{hot rod: } \mathbf{u} = \mathbf{u}_g = 0, \quad \vartheta = \vartheta_g = 1/2, \quad (2.8a,b)$$

$$\text{cold rod: } \mathbf{u} = \mathbf{u}_g = 0, \quad \vartheta = \vartheta_g = -1/2, \quad (2.8c,d)$$

being in contact with the liquid along the faces of the rods and with the gas phase along the cylindrical surface.

(ii) Chamber walls. The outer cylindrical wall and the top and bottom walls of the closed chamber are considered as no-slip and adiabatic boundaries satisfying

$$r = \eta/\Gamma : \quad \mathbf{u}_g = 0, \quad \frac{\partial \vartheta_g}{\partial r} = 0, \quad (2.9a,b)$$

$$z = \pm (1/2 + \Gamma_{rod}/\Gamma) : \quad \mathbf{u}_g = 0, \quad \frac{\partial \vartheta_g}{\partial z} = 0. \quad (2.9c,d)$$

(iii) Liquid–gas interface. The contiguous non-axisymmetric liquid–gas interface is described by a unique radial position  $r = h(\varphi, z, t)$  on which coupling conditions for  $\mathbf{u}$  and  $\vartheta$  must be provided. The continuity of temperature and heat flux requires

$$r = h(\varphi, z, t) : \quad \vartheta = \vartheta_g \quad \text{and} \quad \mathbf{n} \cdot \nabla \vartheta = \tilde{\kappa} \mathbf{n} \cdot \nabla \vartheta_g, \quad (2.10a,b)$$

where  $\mathbf{n}$  is the local unit vector normal to the interface directed from the liquid into the gas phase. The kinematic coupling

$$r = h(\varphi, z, t) : \quad \mathbf{u} = \mathbf{u}_g \quad \text{and} \quad u = \frac{1}{Re} \frac{\partial h}{\partial t} + \frac{v}{r} \frac{\partial h}{\partial \varphi} + w \frac{\partial h}{\partial z}, \quad (2.11a,b)$$

forces material elements on the interface to remain on the interface. Finally, the dynamic condition provided by the tangential stress balance

$$r = h(\varphi, z, t) : \quad \mathbf{n} \cdot \mathbf{S} \cdot \mathbf{t} = -\nabla \vartheta \cdot \mathbf{t} + \tilde{\rho} \tilde{\nu} \mathbf{n} \cdot \mathbf{S}_g \cdot \mathbf{t} \quad (2.12)$$

must be satisfied, where  $\mathbf{S} = \nabla \mathbf{u} + (\nabla \mathbf{u})^T$  and  $\tilde{\rho} \tilde{\nu} \mathbf{S}_g$  are the viscous stress tensors in the liquid and the gas, respectively. The vector  $\mathbf{t}$  can be any of the two orthogonal unit vectors tangent to the interface.

## 2.3. Solution structure

### 2.3.1. Shape of the interface

The non-dimensional radial position  $r = h(\varphi, z, t)$  of the interface is part of the solution and therefore *a priori* unknown. Motivated by the very small capillary numbers  $Ca = \gamma \Delta T / \sigma_0$  in typical experiments, we consider the limit of asymptotically large mean surface tension  $\sigma_0$  in which  $Ca \rightarrow 0$ . In this limit, dynamic free-surface deformations can be neglected, and the problem of determining the liquid–gas interface decouples from solving (2.4) and (2.6) together with (2.8)–(2.12). These circumstances allow for an axisymmetric and stationary interface  $h(\varphi, z, t) \rightarrow h(z)$  that is determined solely by



the normal-stress balance, yielding the Young–Laplace equation

$$\Delta p_h = \frac{\nabla \cdot \mathbf{n}}{Ca} + \frac{Bo}{Ca} z, \quad (2.13)$$

where  $\mathbf{n} = (1, 0, -h_z)^T / \sqrt{1 + h_z^2}$  is the outward surface normal vector,  $\Delta p_h$  is the hydrostatic (subscript  $h$ ) pressure jump across the liquid–gas interface, and

$$Bo = \frac{(\rho_0 - \rho_{g0})gd^2}{\sigma_0} \quad (2.14)$$

is the static Bond number. Note that the ratio  $\lambda = Bd/Bo = \rho_0\beta\sigma_0/[\gamma(\rho_0 - \rho_{g0})]$  is a material parameter. The Young–Laplace equation (2.13) for  $h$  is of second order in  $z$  and  $\varphi$ , and needs to be closed by additional conditions. The pinned contact lines require

$$h(z = \pm 1/2) = \frac{1}{\Gamma}. \quad (2.15)$$

Owing to these constraints, (2.13) has an axisymmetric solution  $h(z)$ , which we consider within its stability limits (Slobozhanin & Perales 1993). To determine  $h(z)$  and the pressure jump  $p_h$  uniquely, (2.13) is solved subject to the volume constraint

$$\Gamma^2 \int_{-1/2}^{1/2} h^2(z) dz = \mathcal{V}, \quad (2.16)$$

where  $\mathcal{V} = V_l/V_0$  is the liquid volume  $V_l$  normalised by the volume  $V_0 = \pi r_i^2 d$  of an upright cylindrical liquid bridge. Within the range of  $\mathcal{V}$  considered, the contact angle is a bijective function of  $\mathcal{V}$  (Nienhüser & Kuhlmann 2002).

### 2.3.2. Basic flow

For a given axisymmetric hydrostatic shape  $h(z)$  of the liquid bridge, the symmetries of the problem allow for a steady axisymmetric flow ( $\partial_t = \partial_\varphi = 0$ ) with  $v_0 = v_{g0} = 0$ , which is denoted  $\mathbf{q}_0(r, z) = (u_0, w_0, p_0, \vartheta_0)$  (liquid phase) and  $\mathbf{q}_{g0}(r, z) = (u_{g0}, w_{g0}, p_{g0}, \vartheta_{g0})$  (gas phase). The pressure fields  $p_{g0}$  and  $p_0$  are flow-induced and add, respectively, to the ambient pressures  $p_a$  (gas) and  $p_a + \Delta p_h$  (liquid).

The flows  $\mathbf{q}_0$  and  $\mathbf{q}_{g0}$  are obtained by solving the steady axisymmetric versions of the differential equations (2.4) and (2.6), subject to the steady axisymmetric versions of the boundary conditions. On  $r = 0$ , axisymmetry requires

$$u_0 = \frac{\partial w_0}{\partial r} = \frac{\partial \vartheta_0}{\partial r} = 0, \quad (2.17)$$

while on the free surface we obtain, from (2.11a,b),

$$\frac{u_0}{w_0} = h_z. \quad (2.18)$$

### 2.3.3. Linear stability analysis

For small Reynolds numbers  $Re$ , the basic flow  $(\mathbf{q}_0, \mathbf{q}_{g0})$  is stable. When  $Re$  exceeds a critical Reynolds number  $Re_c$ , the basic flow becomes unstable. In order to calculate the critical threshold, a linear stability analysis is carried out. To that end, the general three-dimensional time-dependent flow  $\mathbf{q} = (u, v, w, p, \vartheta)$  and  $\mathbf{q}_g = (u_g, v_g, w_g, p_g, \vartheta_g)$  is written as

$$u = u_0(r, z) + u'(r, \varphi, z, t), \quad u_g = u_{g0}(r, z) + u'_g(r, \varphi, z, t), \quad (2.19a,b)$$

$$v = 0 + v'(r, \varphi, z, t), \quad v_g = 0 + v'_g(r, \varphi, z, t), \quad (2.19c,d)$$

$$w = w_0(r, z) + w'(r, \varphi, z, t), \quad w_g = w_{g0}(r, z) + w'_g(r, \varphi, z, t), \quad (2.19e,f)$$

$$p = p_0(r, z) + p'(r, \varphi, z, t), \quad p_g = p_{g0}(r, z) + p'_g(r, \varphi, z, t), \quad (2.19g,h)$$

$$\vartheta = \vartheta_0(r, z) + \vartheta'(r, \varphi, z, t), \quad \vartheta_g = \vartheta_{g0}(r, z) + \vartheta'_g(r, \varphi, z, t), \quad (2.19i,j)$$

where deviations from the basic flow are indicated by a prime ( $'$ ). Inserting this decomposition into (2.4) and (2.6), and linearising with respect to the perturbation quantities, yields the linear stability equations that have the same form,

$$\frac{\partial \mathbf{u}'}{\partial t} + Re(\mathbf{u}_0 \cdot \nabla \mathbf{u}' + \mathbf{u}' \cdot \nabla \mathbf{u}_0) = -\frac{1}{\alpha_\rho} \nabla p' + \alpha_v \nabla^2 \mathbf{u}' + \alpha_\beta B d \vartheta' \mathbf{e}_z, \quad (2.20a)$$

$$\nabla \cdot \mathbf{u}' = 0, \quad (2.20b)$$

$$\frac{\partial \vartheta'}{\partial t} + Re(\mathbf{u}_0 \cdot \nabla \vartheta' + \mathbf{u}' \cdot \nabla \vartheta_0) = \frac{\alpha_\kappa}{Pr} \nabla^2 \vartheta', \quad (2.20c)$$

for both phases. The subscript ‘g’ (for the gas phase) no longer appears, because the distinction between the two phases is made, henceforth, by the set of coefficients  $\alpha$  defined in (2.7).

Due to the homogeneity of (2.20) in  $\varphi$  and  $t$ , the general solution  $\mathbf{q}' = (u', v', w', p', \vartheta')$  of (2.20) can be written as a superposition of normal modes

$$\mathbf{q}' = \sum_{j,m} \hat{\mathbf{q}}_{j,m}(r, z) \exp(\mu_{j,m} t + i m \varphi) + \text{c.c.}, \quad (2.21)$$

where  $\mu = \mu_{j,m} \in \mathbb{C}$  is a complex growth rate, and  $m \in \mathbb{N}_0$  is the azimuthal wavenumber. The index  $j$  numbers the discrete part of the spectrum, and c.c. denotes the complex conjugate. Inserting the ansatz (2.21) into the linear perturbation equations (2.20), one obtains linear differential equations for the perturbation amplitudes  $\hat{\mathbf{q}} = (\hat{u}, \hat{v}, \hat{w}, \hat{p}, \hat{\vartheta})$  that depend only on  $r$  and  $z$ :

$$\begin{aligned} \mu \hat{u} + Re \left[ \left( \frac{1}{r} + \frac{\partial}{\partial r} \right) (2u_0 \hat{u}) + \frac{u_0 i \hat{v} m}{r} + \frac{\partial (u_0 \hat{w} + \hat{u} w_0)}{\partial z} \right] \\ = -\frac{1}{\alpha_\rho} \frac{\partial \hat{p}}{\partial r} + \alpha_v \left[ \frac{1}{r} \frac{\partial}{\partial r} \left( r \frac{\partial \hat{u}}{\partial r} \right) - (m^2 + 1) \frac{\hat{u}}{r^2} - \frac{2}{r^2} i \hat{v} m + \frac{\partial^2 \hat{u}}{\partial z^2} \right], \end{aligned} \quad (2.22a)$$

$m = 0 :$	$\hat{u} = 0$	$\hat{v} = 0$	$\partial \hat{w} / \partial r = 0$	$\partial \hat{\vartheta} / \partial r = 0$
$m = 1 :$	$\partial \hat{u} / \partial r = 0$	$\partial \hat{v} / \partial r = 0$	$\hat{w} = 0$	$\hat{\vartheta} = 0$
$m > 1 :$	$\hat{u} = 0$	$\hat{v} = 0$	$\hat{w} = 0$	$\hat{\vartheta} = 0$

Table 2. Boundary conditions for the perturbation flow on  $r = 0$ .

$$\begin{aligned} \mu \hat{v} + Re \left[ \left( \frac{2}{r} + \frac{\partial}{\partial r} \right) (u_0 \hat{v}) + \frac{\partial(\hat{v} w_0)}{\partial z} \right] \\ = -\frac{1}{\alpha_\rho} \frac{1}{r} \hat{p} i m + \alpha_v \left[ \frac{1}{r} \frac{\partial}{\partial r} \left( r \frac{\partial \hat{v}}{\partial r} \right) - (m^2 + 1) \frac{\hat{v}}{r^2} + \frac{2}{r^2} i \hat{u} m + \frac{\partial^2 \hat{v}}{\partial z^2} \right], \end{aligned} \quad (2.22b)$$

$$\begin{aligned} \mu \hat{w} + Re \left[ \frac{1}{r} \frac{\partial(w_0 \hat{u} + \hat{w} u_0)}{\partial r} + \frac{w_0 i \hat{v} m}{r} + 2 \frac{\partial w_0 \hat{w}}{\partial z} \right] \\ = -\frac{1}{\alpha_\rho} \frac{\partial \hat{p}}{\partial z} + \alpha_v \left[ \frac{1}{r} \frac{\partial}{\partial r} \left( r \frac{\partial \hat{w}}{\partial r} \right) - m^2 \frac{\hat{w}}{r^2} + \frac{\partial^2 \hat{w}}{\partial z^2} \right] + \alpha_\beta B d \hat{\vartheta}, \end{aligned} \quad (2.22c)$$

$$\frac{1}{r} \frac{\partial(r \hat{u})}{\partial r} + \frac{1}{r} i \hat{v} m + \frac{\partial \hat{w}}{\partial z} = 0, \quad (2.22d)$$

$$\begin{aligned} \mu \hat{\vartheta} + Re \left[ \frac{1}{r} \frac{\partial(\vartheta_0 \hat{u} + \hat{\vartheta} u_0)}{\partial r} + \frac{\vartheta_0 i \hat{v} m}{r} + \frac{\partial(\vartheta_0 \hat{w} + \hat{\vartheta} w_0)}{\partial z} \right] \\ = \frac{\alpha_\kappa}{Pr} \left[ \frac{1}{r} \frac{\partial}{\partial r} \left( r \frac{\partial \hat{\vartheta}}{\partial r} \right) - m^2 \frac{\hat{\vartheta}}{r^2} + \frac{\partial^2 \hat{\vartheta}}{\partial z^2} \right]. \end{aligned} \quad (2.22e)$$

Using polar coordinates, the perturbation flow must satisfy boundary conditions on the axis  $r = 0$ . These are provided in [table 2](#) and can be derived from uniqueness conditions for  $\partial \mathbf{u} / \partial \varphi$  and  $\partial \vartheta / \partial \varphi$  as  $r \rightarrow 0$  (Batchelor & Gill 1962; Xu & Davis 1984). Since the imposed constant temperatures on the cylindrical rods are taken care of by the basic flow, all perturbation quantities must vanish on the support rods:

$$\hat{\mathbf{u}} = \hat{\mathbf{u}}_g = 0 \quad \text{and} \quad \hat{\vartheta} = \hat{\vartheta}_g = 0. \quad (2.23a,b)$$

Like the basic flow, the velocity and heat flux of the perturbations must vanish on the solid adiabatic walls of the gas container:

$$\hat{\mathbf{u}}_g = 0 \quad \text{and} \quad \mathbf{n} \cdot \nabla \hat{\vartheta}_g = 0. \quad (2.24a,b)$$

In the limit  $Ca \rightarrow 0$  considered, the liquid–gas interface is indeformable. From (2.10a,b)–(2.12), the coupling on the axisymmetric interface at  $r = h(z)$  between the liquid- and gas-phase perturbations is provided by

$$\hat{\mathbf{u}} = \hat{\mathbf{u}}_g, \quad \hat{\vartheta} = \hat{\vartheta}_g, \quad \mathbf{n} \cdot \nabla \hat{\vartheta} = \tilde{\kappa} \mathbf{n} \cdot \nabla \hat{\vartheta}_g \quad \text{and} \quad \mathbf{n} \cdot \hat{\mathbf{S}} \cdot \mathbf{t} = -\nabla \hat{\vartheta} \cdot \mathbf{t} + \tilde{\rho} \tilde{\mathbf{v}} \mathbf{n} \cdot \hat{\mathbf{S}}_g \cdot \mathbf{t}, \quad (2.25a-d)$$

with  $\hat{\mathbf{S}} = \nabla \hat{\mathbf{u}} + (\nabla \hat{\mathbf{u}})^T$ .

For each azimuthal wavenumber  $m$ , (2.22)–(2.25a–d) represent a linear eigenvalue problem with an infinite number of eigenmodes  $\mathbf{q}'$ . The eigenmodes and the corresponding

eigenvalues

$$\mu_{j,m} = \mu(j, m; Re, \Gamma, \mathcal{V}, Pr, \lambda, \tilde{\rho}, \tilde{v}, \tilde{\kappa}, \tilde{\beta}) \quad (2.26)$$

depend on a number of parameters. Neutral values  $Re_n$  (using subscript  $n$ ) of the Reynolds number associated with each mode  $(j, m)$  are characterised by a vanishing real part (Re) of the eigenvalue,  $\text{Re}[\mu_{j,m}(Re_n)] = 0$ . These conditions define neutral hypersurfaces  $Re_n^{j,m}(\Gamma, \mathcal{V}, Pr, \lambda, \tilde{\rho}, \tilde{v}, \tilde{\kappa}, \tilde{\beta})$  in the parameter space. The envelope of all neutral hypersurfaces  $Re_c = \min_{j,m} Re_n^{j,m}$  is the critical Reynolds number  $Re_c(\Gamma, \mathcal{V}, Pr, \lambda, \tilde{\rho}, \tilde{v}, \tilde{\kappa}, \tilde{\beta})$ . For slightly supercritical Reynolds numbers with  $\epsilon = (Re - Re_c)/Re_c \ll 1$ , the basic flow is guaranteed to be unstable, because at least one eigenmode exists that has a positive growth rate  $\text{Re}(\mu) > 0$ . This does not preclude the rare case of isolated islands in parameter space for larger Reynolds numbers ( $Re/Re_c > 1$ ) for which the basic flow can be linearly stable, i.e. for which  $\forall_{j,m} \text{Re}(\mu_{j,m}) < 0$ . However, within the present linear stability approach, which does not take care of nonlinear effects in the perturbation flow, it cannot be decided if the basic flow  $\mathbf{q}_0$  is stable to finite-amplitude perturbations, either in these linearly stable islands or for  $Re < Re_c$ . Experimental and numerical evidence (Velten *et al.* 1991; Leypoldt *et al.* 2000; Sim & Zebib 2002) suggests, however, that the first instability of the basic flow is typically supercritical.

#### 2.4. Post-processing

Analysing the energy transfer between the basic flow and the neutral mode can provide insights regarding the instability mechanism and helps us to understand the underlying physics. To that end, we build on the energy analysis derived in Nienhüser & Kuhlmann (2002) for a non-cylindrical axisymmetric liquid bridge, where the gas phase was neglected, and extend the equations to the present two-phase model. Multiplying the linearised momentum equation (2.20a) by the perturbation velocity vector  $\mathbf{u}'$ , the resulting equations for the liquid and gas are integrated over the volumes  $V_l$  and  $V_g$ , respectively, occupied by each phase. After splitting all terms into volume and surface integrals by means of Green's theorem, we obtain the balance

$$\frac{dE_{kin}}{dt} = \frac{1}{\mathcal{D}_{kin}} \frac{d}{dt} \int_{V_i} \frac{\mathbf{u}'^2}{2} dV = -1 + M_r + M_\varphi + M_z + \sum_{j=1}^5 I_j + B, \quad i \in [l, g], \quad (2.27)$$

for the (normalised) rate of change of the kinetic energy  $E_{kin}$ , where all terms on the right-hand side have been normalised by the mechanical dissipation rate  $\mathcal{D}_{kin}$ . Similarly, multiplication of (2.20c) by  $\vartheta'$  and integration over the volume occupied by each phase yields the thermal energy balance

$$\frac{dE_{th}}{dt} = \frac{1}{\mathcal{D}_{th}} \frac{d}{dt} \int_{V_i} \frac{\vartheta'^2}{2} dV = -1 + \sum_{j=1}^2 J_j + H_{fs}, \quad i \in [l, g], \quad (2.28)$$

where all terms now have been scaled by the thermal dissipation rate  $\mathcal{D}_{th}$ . Thus the scaled dissipation rates  $D_{kin} = D_{th} = 1$  are constant. The subscripts  $l$  and  $g$  have been omitted for all terms arising in (2.27) and (2.28) with the understanding that the balances are valid separately for both the liquid and gas phases. Detailed expressions for the individual terms are provided in Appendix A. The terms  $\sum I_j = \sum \int i_j dV$  and  $\sum J_j = \sum \int j_j dV$  (see (A2)) represent the scaled total production rates of kinetic and thermal

Fluid	$\rho$ (kg m <sup>-3</sup> )	$\nu$ (m <sup>2</sup> s <sup>-1</sup> )	$\kappa$ (m <sup>2</sup> s <sup>-1</sup> )	$\sigma_0$ (N m <sup>-1</sup> )	$\gamma$ (N m <sup>-1</sup> K <sup>-1</sup> )	$\beta$ (K <sup>-1</sup> )
2 cSt	871	$2.00 \times 10^{-6}$	$7.14 \times 10^{-8}$	$18.3 \times 10^{-3}$	$7 \times 10^{-5}$	$1.24 \times 10^{-3}$
Air	1.184	$1.56 \times 10^{-5}$	$2.22 \times 10^{-5}$			$3.38 \times 10^{-3}$

Table 3. Thermophysical properties of the working fluids 2 cSt silicone oil KF96L-2cs and air at 25 °C.

energy, respectively, which is transferred between the basic and perturbation flows, with corresponding local production densities  $i_j$  and  $j_j$ . The terms  $M_r$ ,  $M_\varphi$  and  $M_z$  in the kinetic energy balance (2.27) represent the work done per unit time by Marangoni forces in the respective spatial directions. Furthermore, the contribution  $B$  (see (A4)) accounts for the work done per unit time by buoyancy forces. In the thermal budget (2.28),  $H_{fs}$  (see (A5)) denotes the heat transferred through the liquid–gas interface. It appears in the budgets for both the liquid and gas phases, albeit with opposite signs.

It is generally accepted to refer to  $E_{th}$  and  $E_{th,g}$  as thermal energies, even though it contradicts the definition of the thermodynamic thermal energy. Hence, what we call thermal energy is rather a measure for the temperature deviation from the axisymmetric temperature field.

## 2.5. Reference case and parameter variation

Due to the large number of parameters governing the linear stability problem, it is computationally too demanding to cover the whole parameter space. Therefore, we consider the liquid–gas couple made of 2 cSt silicone oil (KF96L-2cs, Shin-Etsu Chemical Co., Ltd., Japan) and air with constant material parameters, evaluated at  $T_0 = 25$  °C for both fluids. This selection determines the non-dimensional material parameters  $Pr$ ,  $\lambda$ ,  $\tilde{\rho}$ ,  $\tilde{\nu}$ ,  $\tilde{\kappa}$  and  $\tilde{\beta}$ . The thermophysical properties of both working fluids are listed in table 3.

Furthermore, we keep the aspect ratio of the support rods as well as the chamber radius ratio constant at  $\Gamma_{rod} = 0.4$  and  $\eta = 4$ , respectively. This configuration corresponds to the experiments carried out by Romanò *et al.* (2017). We are left with the important geometrical parameters  $\mathcal{V}$  and  $\Gamma$  representing the volume of liquid and the geometric aspect ratio of the liquid bridge, respectively. Finally, the gravity level can be varied via the Bond number  $Bd$ .

The origin of all parameter variations is a common reference case. It is based on the experimental geometry investigated by Romanò *et al.* (2017) with support rods of radius  $r_i = 2.5$  mm and terrestrial gravity. Different from our objectives, however, Romanò *et al.* (2017) kept the temperature difference constant at  $\Delta T = 10$  K  $< \Delta T_c$ , which is far subcritical. We define the reference case by  $\Gamma_{ref} = 0.66$ ,  $\mathcal{V}_{ref} = 1$  and  $Bd_{ref} = 0.41$ . All reference parameters are collected in table 4. Starting from the reference case, we perform three parameter variations.

- (i) A first variation, which is typically made in laboratory experiments, is a variation of the length  $d$  of the liquid bridge (Velten *et al.* 1991; Monti, Savino & Lappa 2000; Nienhüser & Kuhlmann 2003; Melnikov *et al.* 2015), corresponding to a variation of  $\Gamma$ . Owing to the dependence of  $Bd \sim d^2$ , we simultaneously vary  $Bd$  such that  $Bd = Bd_{ref}(\Gamma/\Gamma_{ref})^2$ , corresponding to a constant acceleration of gravity. The range of variation is  $\Gamma \in [0.5, 1.8]$  and  $Bd \in [0.236, 3.07]$ .

$\Gamma_{ref}$	$\mathcal{V}_{ref}$	$Bd_{ref}$	$Pr$	$\lambda$	$\tilde{\rho}$	$\tilde{\nu}$	$\tilde{\kappa}$	$\tilde{\beta}$
0.66	1	0.41	28	0.32	$1.36 \times 10^{-3}$	7.80	310.16	2.73

 Table 4. Constant non-dimensional parameters;  $\Gamma$ ,  $\mathcal{V}$  and  $Bd$  are varied around the reference values given.

- (ii) In a second series of calculations, we vary  $\mathcal{V} \in [0.65, 1.3]$  for  $\Gamma = \Gamma_{ref}$  and  $Bd = Bd_{ref}$ . This type of variation has also been used in experiments (Hu *et al.* 1994; Sakurai *et al.* 1996; Tang & Hu 1999; Nienhüser & Kuhlmann 2002; Yano *et al.* 2016).
- (iii) In a third step, we vary the acceleration of gravity for  $\Gamma = \Gamma_{ref}$  and  $\mathcal{V} = \mathcal{V}_{ref}$ . In this series of calculations, the Bond number is varied in the range  $Bd \in [-1.25, 1.25]$ . This variation is intended to show how the instabilities for heating from above (reference case) and below are related to each other and to the case of zero gravity in which buoyancy forces and hydrostatic pressure are eliminated (Velten *et al.* 1991; Wanschura, Kuhlmann & Rath 1997b; Kawamura *et al.* 2012).

### 3. Numerical methods

To compute the basic state and its linear stability, a revised version of the numerical code MaranStable (Kuhlmann, Lukasser & Muldoon 2011; Stojanovic & Kuhlmann 2020b) is used. It is based on an earlier version developed by M. Lukasser (see § 4.2 of Shevtsova *et al.* 2014).

#### 3.1. Shape of the interface

In a first step, the static axisymmetric shape  $h(z)$  of the liquid–gas interface is computed. To that end, the Young–Laplace equation (2.13) is reformulated as a system of two ordinary differential equations:

$$h_{zz} = (1 + h_z^2) \left[ \frac{1}{h} - (Ca \Delta p_h - Bo z) \sqrt{1 + h_z^2} \right], \quad (3.1a)$$

$$\Delta p_{h,z} = 0, \quad (3.1b)$$

where the subscript  $z$  denotes differentiation with respect to  $z$ . These equations, together with the pinning conditions (2.15), represent a boundary value problem, which is discretised by central finite differences on a uniform mesh. The pressure jump  $\Delta p_h$  is determined by the volume constraint (2.16). The discretised set of nonlinear equations is solved using the Newton–Raphson method. The iteration is terminated as soon as both the  $L_\infty$  and  $L_2$  norms of the residual have dropped below  $10^{-6}$ .

#### 3.2. Basic flow

The steady axisymmetric versions of the nonlinear equations (2.4) and (2.6) determining the basic state are discretised on a structured and staggered grid using second-order finite volumes (Wesseling 2009). In order to implement the boundary conditions on the liquid–gas interface, the grid is body-fitted to the interface, transforming the radial coordinate to  $\xi = r/h(z)$ . To perform this transformation, the previously determined



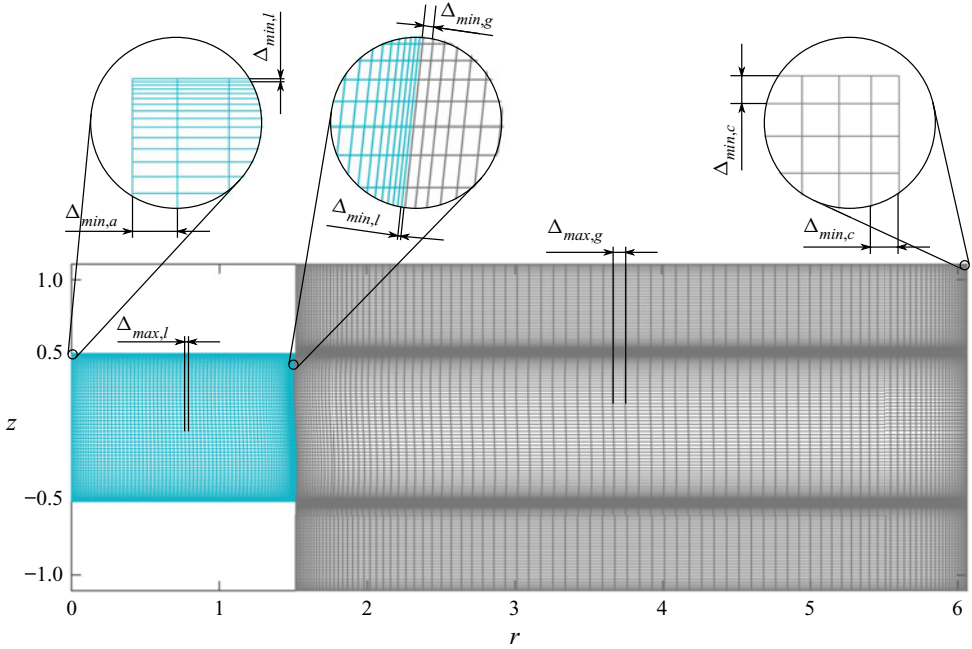


Figure 2. Example for the physical mesh inside the liquid (light blue) and the gas (grey). For better visualisation, the total number of nodes was reduced to  $N_{tot} = 18\,852$ , which is a reduction of more than 80 % compared to the mesh used for the calculations.

$h(z)$  is interpolated to the current grid using splines. Furthermore, the grid is refined towards all boundaries using a hyperbolic-tangent profile (Thompson, Warsi & Mastin 1985). Inside the liquid, a minimum cell width of  $\Delta_{min,l} = 5 \times 10^{-5}$  was chosen for the wall-bounded cells and along the interface in order to guarantee that thermal boundary layers will be resolved for all calculations. On the axis of symmetry (subscript  $a$ ), moderate temperature and velocity gradients are expected, justifying the larger minimum cell width in radial direction  $\Delta_{min,a} = 10^{-3}$ . The spatial resolution in the gas phase was set to  $\Delta_{min,g} = 3\Delta_{min,l}$  along the interface, and  $\Delta_{min,c} = 10^{-3} \times \Gamma_{rod}/\Gamma$  close to the adiabatic chamber walls (subscript  $c$ ). The cells are stretched towards the interior with a stretching factor  $f = 1.15$  until maximum cell widths  $\Delta_{max,l} = 0.0075 = 150 \Delta_{min,l}$  and  $\Delta_{max,g} = 0.02(\eta - 1)/\Gamma = 150 \Delta_{min,c} \approx 600 \Delta_{min,g}$  are reached in the bulk of the liquid and the gas, respectively. These conditions lead to a total of  $N_{tot} = 103\,613$  cells, of which  $N_r \times N_z = 244 \times 197$  cells belong to the liquid, and  $N_r \times N_z = 115 \times 483$  cells belong to the gas phase. Figure 2 shows the physical mesh, but at much lower resolution than used for the actual calculations.

The nonlinear algebraic equations resulting from the discretisation are solved by Newton–Raphson iteration:

$$\mathbf{J}(\mathbf{q}_0^{(k)}) \cdot \delta \mathbf{q} = -\mathbf{f}(\mathbf{q}_0^{(k)}), \quad (3.2a)$$

$$\mathbf{q}_0^{(k+1)} = \mathbf{q}_0^{(k)} + \delta \mathbf{q}, \quad (3.2b)$$

where  $\delta \mathbf{q}$  is the increment of the approximation of the basic flow from the  $k$ th to the  $(k + 1)$ th iteration step. Inserting (3.2b) into the steady axisymmetric versions of (2.4)

and (2.6) yields the equations governing  $\delta \mathbf{q}$ :

$$\begin{aligned} & Re(\delta \mathbf{u} \cdot \nabla \mathbf{u}_0^{(k)} + \mathbf{u}_0^{(k)} \cdot \nabla \delta \mathbf{u}) + \frac{1}{\alpha_\rho} \nabla \delta p - \alpha_v \nabla^2 \delta \mathbf{u} - \alpha_\beta B d \delta \vartheta \mathbf{e}_z \\ &= -Re \mathbf{u}_0^{(k)} \cdot \nabla \mathbf{u}_0^{(k)} - \frac{1}{\alpha_\rho} \nabla p_0^{(k)} + \alpha_v \nabla^2 \mathbf{u}_0^{(k)} + \alpha_\beta B d \vartheta_0^{(k)} \mathbf{e}_z, \end{aligned} \quad (3.3a)$$

$$\nabla \cdot \delta \mathbf{u} = -\nabla \cdot \mathbf{u}_0^{(k)}, \quad (3.3b)$$

$$\delta \mathbf{u} \cdot \nabla \vartheta_0^{(k)} + \mathbf{u}_0^{(k)} \cdot \nabla \delta \vartheta - \frac{\alpha_k}{Ma} \nabla^2 \delta \vartheta = -\mathbf{u}_0^{(k)} \cdot \nabla \vartheta_0^{(k)} + \frac{\alpha_k}{Ma} \nabla^2 \vartheta_0^{(k)}, \quad (3.3c)$$

where the nonlinear terms have been linearised with respect to  $\delta \mathbf{q}$ . The Jacobian operator  $\mathbf{J}(\mathbf{q}_0^{(k)})$  and the nonlinear residual  $-\mathbf{f}(\mathbf{q}_0^{(k)})$  are identified readily from (3.3). The Newton iteration (3.2) is considered converged as soon as both the infinity norm  $\|\delta \mathbf{q}\|_\infty$  and the  $L_2$  norm  $\|\delta \mathbf{q}\|_2$  of the residual have dropped below  $10^{-6}$ .

### 3.3. Linear stability of the basic flow

Once the basic state  $\mathbf{q}_0$  is computed, it parametrically enters the linear stability equations (2.22), which are discretized on the same mesh using the same finite volume method. The resulting large generalised complex eigenvalue problem is converted into a generalised eigenvalue problem with real matrices by introducing  $\tilde{\nu} = i\hat{\nu}$  (Theofilis 2003). Defining the decay rate  $\chi = -\mu$ , the generalised real eigenvalue problem has the form

$$\mathbf{A} \cdot \hat{\mathbf{q}} = \chi \mathbf{B} \cdot \hat{\mathbf{q}}, \quad (3.4)$$

where  $\mathbf{B}$  is singular. For a Reynolds number  $Re \approx Re_n$  close to a neutral stability boundary (subscript  $n$ ), the most dangerous modes (numbered by  $i$ ) belong to the eigenvalues  $\chi_i$  with the smallest real parts, satisfying  $\text{Re}(\chi_i) \approx 0$ . To find the most dangerous eigenvalue, i.e. the one with the smallest real part of  $\chi$ , twelve eigenvalues  $\tilde{\chi}_i$  with the smallest absolute value are computed, in a first step, via an implicitly restarted Arnoldi method implemented in ARPACK (Lehoucq, Sorensen & Yang 1998) and available under MATLAB. A Krylov subspace of dimension  $K = 100$  is employed. Based on the eigenvalue  $\tilde{\chi}_{sr}$  with the smallest real part among the twelve eigenvalues  $\tilde{\chi}_i$ , i.e.  $\tilde{\chi}_{sr} : \text{Re}(\tilde{\chi}_{sr}) = \min[\text{Re}(\tilde{\chi}_i)]$ , we adopt the method proposed by Meerbergen, Spence & Roose (1994) to validate that the eigenvalue  $\tilde{\chi}_{sr}$  is indeed the one with the smallest real part among all the eigenvalues  $\chi_i$  and not only among the twelve eigenvalues  $\tilde{\chi}_i$  with the smallest absolute value. To that end, 17 eigenvalues  $\zeta = (\chi - a_2)(\chi - a_1)$  with the largest magnitude of the Cayley transform

$$(\mathbf{A} - a_2 \mathbf{B}) \cdot \hat{\mathbf{q}} = \zeta (\mathbf{A} - a_1 \mathbf{B}) \cdot \hat{\mathbf{q}} \quad (3.5)$$

are computed, as described in Meerbergen *et al.* (1994). The parameters  $a_1$  and  $a_2$  are determined by the five real eigenvalues with the smallest absolute value and a user-defined parameter  $b = |(\chi_i - a_2)/(\chi_i - a_1)| = 1.2$ , where  $\chi_i$  is one of the eigenvalues with the smallest real part. The resulting 17 eigenvalues containing the most dangerous mode are then sorted according to the magnitudes of their real parts.

At the neutral Reynolds number  $Re_n$ , the real part of the eigenvalue of the most dangerous mode, identified from the above procedure, crosses zero. To determine  $Re_n$  for a given azimuthal wavenumber  $m$ , the Reynolds number is varied in small steps, typically by approximately 5 % of its value, until the sign of  $\min_i \text{Re}(\chi_i)|_m$  changes, signalling that at least one root exists within this interval of  $Re$ . The root  $Re_n$  is then computed

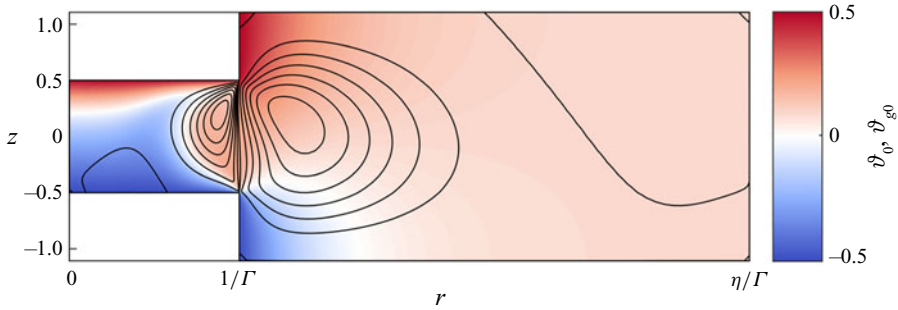


Figure 3. Streamlines and temperature fields  $\vartheta_0$  and  $\vartheta_{g0}$  (colour) of the basic state for the reference case ( $\Gamma = 0.66$ ,  $\mathcal{V} = 1$ ,  $Bd = 0.41$ ) at criticality  $Re_c = 731$ . Streamline levels differ in the liquid and the gas, but they are drawn equidistantly in each phase.

by the bisectioned direct quadratic *regula falsi* as described in Gottlieb & Thompson (2010), using the convergence condition  $|\min_i \operatorname{Re}(\chi_i)|_m| < 10^{-5}$ , i.e. a sufficiently small absolute value of the growth rate's real part. Repeating this procedure for a series of wavenumbers  $m = 0, 1, 2, \dots, M$  allows us to detect the critical Reynolds number  $Re_c$  as the envelope gathering the lowest neutral Reynolds numbers over all  $Re_n(m)$ .

In order to track the neutral curves under a variation of one of the parameters  $\Gamma$ ,  $\mathcal{V}$  or  $Bd$ , a natural continuation technique is used. The converged basic state and neutral Reynolds number are used as initial conditions for the Newton iteration to compute the basic state for the incremented parameter, followed by solving the new eigenvalue problem. The step change of the parameter is typically 1 % of its value. If necessary, the parameter variation is refined, e.g. near intersection points of neutral curves or when  $Re_n$  depends sensitively on the parameter varied.

The numerical code has been tested extensively. Grid convergence, verification and validation are described in detail in Appendix B.

## 4. Results

### 4.1. Reference case

#### 4.1.1. Basic flow

Since the basic two-dimensional flow enters the linear stability analysis parametrically, it is important to examine its characteristics closely. Figure 3 shows the streamlines and the temperature field at criticality for the reference case ( $\Gamma = 0.66$ ,  $\mathcal{V} = 1$ ,  $Bd = 0.41$ ). The hydrostatic shape of the interface deviates only slightly from the cylindrical shape. The thermocapillary stresses along the interface, directed from the hot corner to the cold one, lead to a streamline crowding at the interface and drive a clockwise vortex in the liquid phase (figure 3). Even though the absolute Rayleigh number for the liquid phase is  $|Ra| = |Pr Bd Re| = 8392$ , buoyancy forces do not cause the instability, because of the overall stable thermal stratification (see also Wanschura *et al.* 1997b). Buoyancy forces are, however, responsible for the vortex in the liquid, which is more slender than under zero gravity, because the hot fluid transported near the free surface to the cold wall has the tendency to rise in the bulk. This causes the large separation bubble on the cold wall (Romanò & Kuhlmann 2018), also visible in figure 3.

Owing to the geometry of the gas space, a much larger vortex is created in the gas phase (counterclockwise in figure 3). Because the thermal diffusivity of the gas is much higher

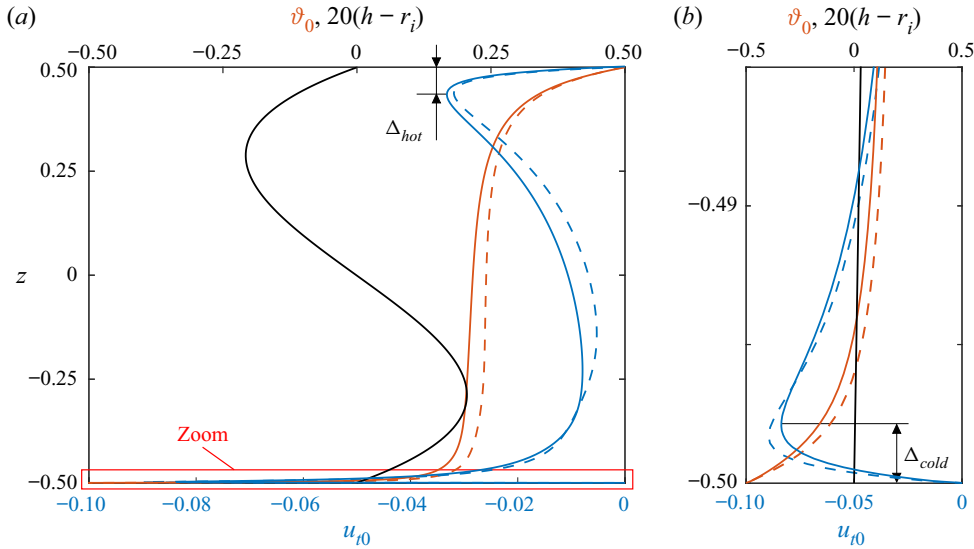


Figure 4. Tangential velocity  $u_{t0} = \mathbf{t} \cdot \mathbf{u}_0$  (solid blue lines) and temperature distribution  $\vartheta_0$  (solid red lines) of the basic flow along the free surface (parametrised by  $z$ ) for the reference case at criticality ( $\Gamma = 0.66$ ,  $\mathcal{V} = 1$ ,  $Bd = 0.41$ ,  $Re = Re_c = 731$ ). Also shown, as dashed lines, are the corresponding profiles for the single-fluid model at the same Reynolds number, and for an adiabatic free surface, neglecting viscous stresses from the gas. (a) Profiles along the whole free surface. (b) Zoom into the red rectangle shown in (a). The black curve indicates the shape  $h(z)$  of the interface.

than that of the liquid (table 4), the convective effect on the temperature distribution in the gas phase is very weak. The temperature distribution along the interface (figure 4), being larger than  $T_0$  on average, causes a mean temperature  $\vartheta_{g0} > 0$  in the gas phase far away from the liquid bridge. Furthermore, a weak flow arises in a large separation bubble, while much smaller viscous eddies can be identified close to all four corners of the annular gas container. Buoyancy in the gas phase is even weaker than in the liquid phase. The ratio  $Ra_g/Ra = \tilde{\beta}\tilde{d}^3/(\tilde{\nu}\tilde{\kappa}) \approx 10^{-2}$ , where  $\tilde{d} = 1 + 2\Gamma_{rod}/\Gamma$ , suggests that buoyancy is negligible in the gas.

The distributions of the velocity (blue) and temperature (red) on the free surface are shown in figure 4(a) for the reference case (solid lines). Also shown are the profiles for the single-fluid model with an adiabatic free surface (dashed lines), neglecting viscous stresses from the gas. For both models, the boundary layer character is obvious from the steep variation of the temperature near the hot and cold corners. Associated with the temperature gradients are peaks of the surface velocity very close to the hot and cold corners. Of these, the cold-corner peak is particularly sharp, because the fluid at the interface is accelerated towards the wall, where it must get decelerated to zero. Since the finite volume method employed does not require any regularisation of the boundary conditions near the corners, the velocity peaks are fully resolved (zoom in figure 4b). The temperature is almost constant along the free surface midway between the two surface velocity peaks (figure 4b) as well as inside the main vortex in the liquid (figure 3). The two-fluid model exhibits a lower surface temperature in the plateau region than the adiabatic single-fluid model. This indicates that the two-fluid model exhibits a heat loss, i.e. a net heat flux outwards through the free surface (free-surface Nusselt number  $Nu_{fs} < 0$  defined in (B2)), a stronger thermocapillary driving along the hotter part of the interface as compared to the

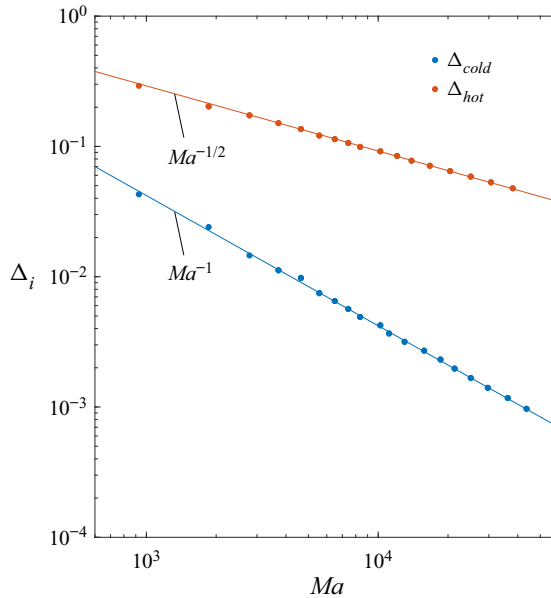


Figure 5. Distances  $\Delta_i$  of the surface velocity peaks of the basic flow from the cold corner (blue dots,  $i = \text{cold}$ ) and the hot corner (red dots,  $i = \text{hot}$ ) compared to the theoretical scalings of the respective thermal boundary layer thicknesses (lines).

single-fluid model, and thus a larger surface velocity along most parts of the free surface. As a consequence, the flow obtained with the adiabatic single-fluid model is approximately twice as stable than the one obtained with the two-fluid model for the same conditions; cf. figure 29 in § B.1.

For high-Prandtl-number flows, the thermal boundary layers in the liquid near the hot and cold corners, i.e. on the circular rigid end walls and at the interface, are more relevant than the viscous boundary layers. For pure thermocapillary flow in the single-fluid model with contact angle  $\alpha = 90^\circ$ , the thermal boundary layer thickness on the cold wall near the contact line is expected to scale  $\sim Ma^{-1}$  in the viscous convective limit ( $Ma \rightarrow \infty$ ,  $Re \ll Ma$ ) (Canright 1994). On the hot wall, the thermal boundary layer thickness should scale  $\sim Ma^{-1/2}$  in this limit (Kamotani & Ostrach 1998). The thickness of the thermal boundary layers can be measured by the distances  $\Delta_{hot}$  and  $\Delta_{cold}$  of the velocity peaks from the hot and cold corners, respectively. Both distances are shown in figure 5 as functions of  $Ma$  for the present two-fluid model. The locations of the velocity peaks  $\Delta_{hot}(Ma)$  and  $\Delta_{cold}(Ma)$  exhibit the same scaling with  $Ma$  as predicted theoretically for the single-fluid model in the viscous convective limit.

#### 4.1.2. Hydrothermal wave instability

At  $Re_c = 731$ , the basic flow becomes unstable with respect to a pair of azimuthally propagating modes with  $\omega_c = \text{Im}(\gamma_c) = \pm 14.85$  and  $m = 3$ . One of the two critical modes is illustrated in figure 6. The global temperature distribution in the horizontal plane at  $z = 0.20$  shown in figure 6(a) indicates that the temperature perturbations arise essentially in the liquid phase, while the gas phase temperature perturbations are weak. A close-up, including the velocity vector field, is shown figure 6(b). It reveals the characteristic structures of the internal perturbation temperature field and axial vortices known from

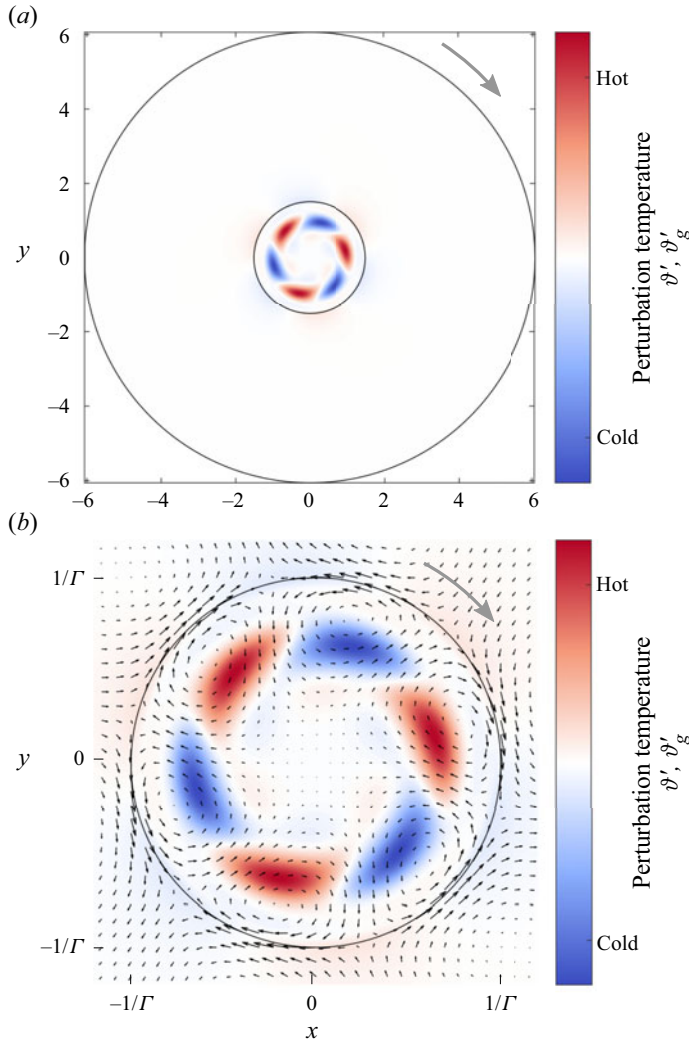


Figure 6. Critical velocity field (black arrows) and critical temperature field (colour) for the reference case ( $Re_c = 731$ ,  $m_c = 3$ ) in the horizontal plane  $z = 0.20$  in which the local thermal production  $\vartheta' \mathbf{u}' \cdot \nabla \vartheta_0$  takes its maximum in the bulk of the liquid. The grey arrow indicates the rotation direction of the mode. (a) Complete domain. (b) Close-up of the liquid phase.

smaller Prandtl numbers (Wanschura *et al.* 1995). The perturbation vortices are driven in the azimuthal direction by the mainly azimuthal temperature gradients on the free surface (figure 7). These vortices transport cold (hot) fluid (note the basic state temperature distribution shown in figure 3) from the interior (from the free surface) just ahead of the cold (hot) interior perturbation temperature extrema, thus feeding the existing extrema and determining the azimuthal direction of propagation (indicated by the grey arrow) of the wave. The perturbation flow, on the other hand, is maintained by radial conduction of perturbation temperature from the internal extrema to the free surface such that the (mainly axial) perturbation vortices seen in figure 6(b) are driven by (mainly azimuthal) thermocapillary stresses. The structure of the perturbation flow confirms its character as a hydrothermal wave (Smith & Davis 1983a; Wanschura *et al.* 1995).



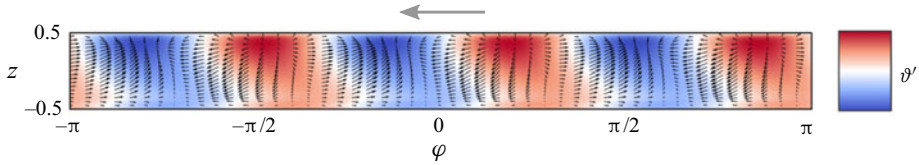


Figure 7. Critical mode (black arrows, colour) for the reference case evaluated on the free surface and projected radially ( $Re_c = 731$ ,  $m_c = 3$ ). The arrow indicates the direction of propagation.

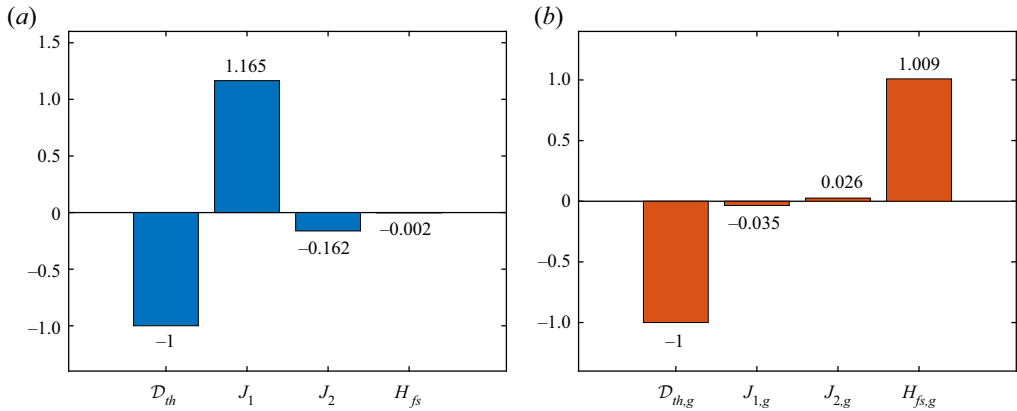


Figure 8. Thermal energy budget of the critical mode for the reference case ( $Re_c = 731$ ,  $m_c = 3$ ). (a) Liquid phase. (b) Gas phase.

The relevance of the temperature transport described is also confirmed by the total thermal energy budgets shown in figure 8. From figure 8(a), thermal perturbation energy in the liquid phase is produced mainly by  $J_1$  (production due to radial convection of basic state temperature; see (A2b)) and dissipated in the bulk. Note that the instability cannot be due to axial temperature gradients, because their total contribution to the thermal energy budget is negative:  $J_2 < 0$ . Only a very small fraction of thermal perturbation energy ( $H_{fs}$ ) is lost to the gas phase (in accordance with figure 6a), which appears as the major source term  $H_{fs,g} = -H_{fs}(\mathcal{D}_{th}/\mathcal{D}_{th,g})$  in the gas phase (figure 8b) and which gets dissipated readily. In the present two-phase system with a cylindrical gas confinement, the gas phase thus merely plays a passive role when it comes to the instability mechanism. Moreover, due to the very high Prandtl number, inertial effects are not causing the instability (Wanschura *et al.* 1995). Likewise, buoyancy is not of key importance for the instability for the reference case (for stronger buoyancy, see Wanschura *et al.* 1997b).

The three-dimensional structure of the travelling temperature perturbation field and of the total thermal energy production is shown by isosurfaces in figure 9. A cross-section at an azimuthal angle at which the local thermal energy production in the bulk reaches its maximum is shown in figure 10. It is seen that the thermal energy production is strong where large interior gradients of the basic temperature field arise, i.e. near the region  $\vartheta_0 \approx 0$  (white colour in figure 3), which is aligned with the streamlines on the interior side of the basic vortex in the liquid phase. Further, from figure 9, one can notice that the perturbation temperature isosurfaces and those for the energy production form an approximate spiral around the basic vortex. The phase relation between the internal temperature perturbations and the thermal energy transfer rate  $j$  is shown in

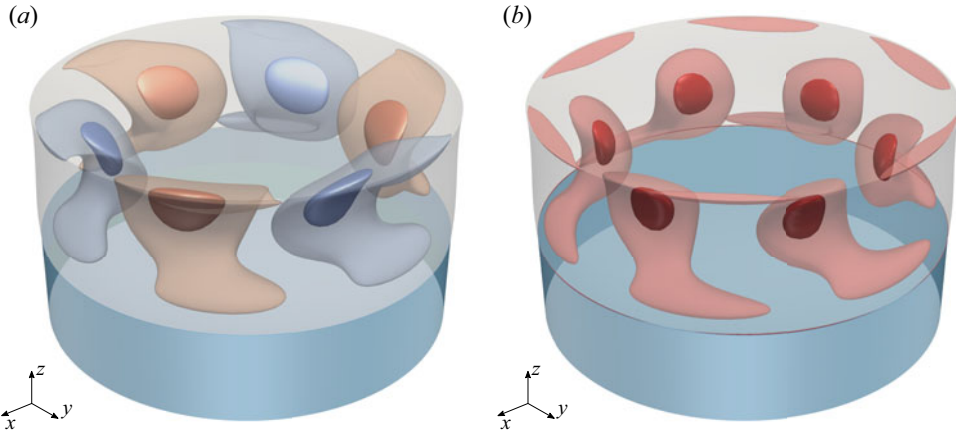


Figure 9. (a) Contours of the perturbation temperature  $\vartheta'$  in the liquid. The isosurface values are  $\pm 0.25 \times \max |\vartheta'|$  (light colours) and  $\pm 0.75 \times \max |\vartheta'|$  (dark colours). (b) Contours of the local thermal production rate  $j_1 + j_2 = \vartheta' \mathbf{u}' \cdot \nabla \vartheta_0$  shown at the isosurface values  $0.1 \times \max |\vartheta' \mathbf{u}' \cdot \nabla \vartheta_0|$  (light red) and  $0.7 \times \max |\vartheta' \mathbf{u}' \cdot \nabla \vartheta_0|$  (dark red).

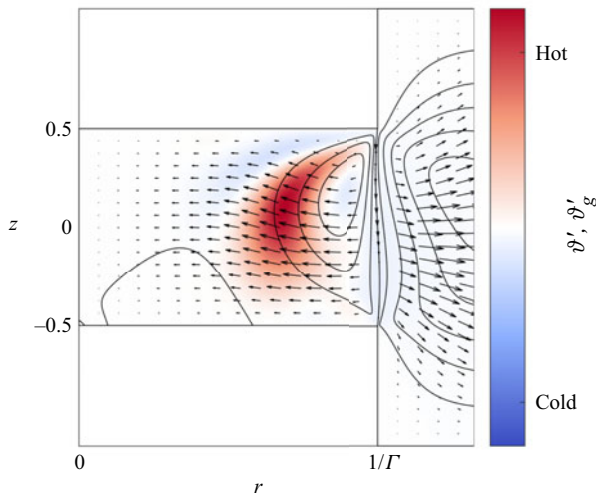


Figure 10. Critical mode  $m_c = 3$  for the reference case at  $Re_c = 731$ . Shown are streamlines of the basic flow, the critical velocity field (arrows) and the critical temperature field (colour) in the  $(r, z)$  plane in which the local thermal production  $\vartheta' \mathbf{u}' \cdot \nabla \vartheta_0$  takes one of its maxima in the bulk.

figure 11 for  $z = 0.20$ . Similar to the  $Pr = 4$  case (Wanschura *et al.* 1995), the thermal perturbation energy is created just ahead of the instantaneous perturbation temperature extrema, consistent with the clockwise propagation of the hydrothermal wave.

We find that the critical Reynolds number for the single-fluid model and  $\Gamma = 0.66$ ,  $\mathcal{V} = 1$ ,  $Bo = 0.41$  is more than twice that for the present two-fluid model (see also figure 29 in § B.1). The basic flow for the single-fluid model with adiabatic interface exhibits a higher surface temperature than the two-fluid model. This might suggest that the radial basic state temperature gradients are higher for the single-fluid model, thus providing a better source of energy for the instability. This effect, however, is counteracted by the lower surface and

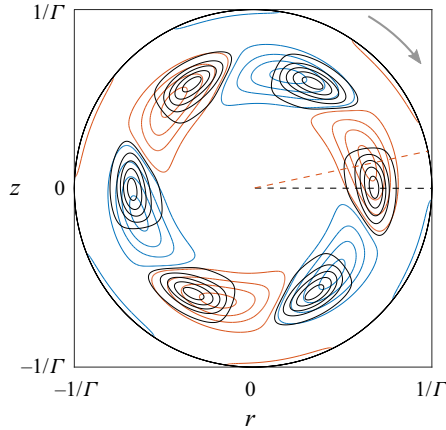


Figure 11. Isolines of the positive (red) and negative (blue) perturbation temperature, and of the local production density  $j = j_1 + j_2$  (black) in the horizontal plane  $z = 0.20$ . Dashed lines are central lines through the maxima of the perturbation temperature (red) and of the related energy transfer (black). The grey arrow indicates the rotation direction of the mode.

return-flow velocity (figure 4), which tends to reduce the radial temperature gradients at midplane. While we cannot pinpoint exactly the reason for the large difference in  $Re_c$ , we notice that the critical temperature field in case of the single-fluid model is distinct from that of the present two-fluid model, exhibiting a finer structure with a much more pronounced spiral character (not shown, but similar to the mode for  $Pr = 68$  reported in Stojanovic & Kuhlmann 2020a). It is thus expected that the relative importance of the thermal dissipation for the critical mode in the single-fluid model is considerably larger than for the critical mode of the two-fluid model, resulting in a considerable stabilisation of the basic flow in the single-fluid model.

#### 4.2. Dependence of the linear stability boundary on the length of the liquid bridge

Figure 12 shows the dependence of the critical Reynolds number  $Re_c$  (figure 12a) and the critical oscillation frequency  $\omega_c$  (figure 12b) on the length of the liquid bridge, expressed by the aspect ratio  $\Gamma$ . The relative volume of the liquid bridge is kept constant at  $\mathcal{V} = \mathcal{V}_{ref} = 1$  and  $Bd = Bd_{ref} \times (\Gamma/\Gamma_{ref})^2$ . In addition, neutral Reynolds numbers and associated neutral frequencies are displayed as thin lines for  $Re > Re_c$ . The critical azimuthal wavenumber  $m$  is coded by colour.

Within the range of  $\Gamma$  considered, only critical modes with  $m = 1$ ,  $m = 3$  and  $m = 4$  arise. The aspect ratios at which the critical mode changes are  $\Gamma^{3,4} = 0.5590$  ( $m = 3 \leftrightarrow 4$ ) with  $Re_c(\Gamma^{3,4}) = 643.1$ , and  $\Gamma^{1,3} = 0.9020$  ( $m = 1 \leftrightarrow 3$ ) with  $Re_c(\Gamma^{1,3}) = 1645.9$ . We find the basic flow to be particularly stable near  $\Gamma^{1,3}$ . The variation of the critical wavenumber with  $\Gamma$  follows the well-known trend according to which  $m_c$  decreases as  $\Gamma$  increases (as the liquid bridge becomes longer). For  $Pr = 7$ , Preisser *et al.* (1983) found experimentally that  $m_c \approx 2.2/\Gamma$  (for  $Pr = 28$ ; see also Ueno *et al.* (2003), and others). A mode with  $m = 2$  does not become critical in the range of  $\Gamma$ . But near  $\Gamma = 0.9$ , the many neutral Reynolds numbers do not differ much, with  $Re_n(m = 1) = 1690$ ,  $Re_n(m = 2) = 1681$  and  $Re_c(m = 3) = 1635$ , such that a complicated supercritical dynamics can be expected near this aspect ratio.

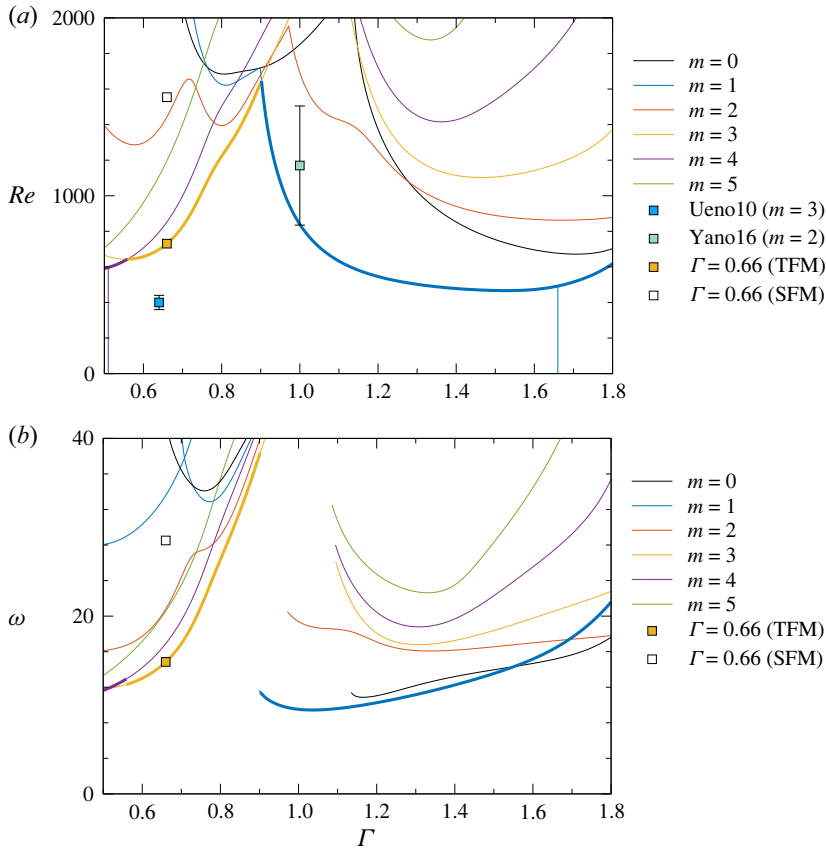


Figure 12. (a) Neutral Reynolds numbers (thin lines) and critical Reynolds numbers  $Re_c$  (thick lines) as functions of the aspect ratio  $\Gamma$  for  $\mathcal{V} = 1$  and  $Bd = Bd_{ref} \times (\Gamma/\Gamma_{ref})^2$ . (b) Corresponding neutral (thin lines) and critical (thick lines) frequencies  $\omega$ . The wavenumbers (colour), symbols and abbreviations are explained in the legend, with TFM meaning two-fluid model, SFM meaning adiabatic single-fluid model, Ueno10 meaning Ueno & Torii (2010), and Yano16 meaning Yano *et al.* (2016).

In addition to the critical mode for the reference case  $\Gamma = 0.66$  with  $m_c = 3$  discussed above, two other critical modes are visualised in figures 13 and 14 for a short ( $\Gamma = 0.51$ ,  $m_c = 4$ ) and a long ( $\Gamma = 1.66$ ,  $m_c = 1$ ) liquid bridge, respectively. These aspect ratios are indicated in figure 12(a) by vertical thin lines. Note that the interface is deformed in both cases. However, the static surface deformation is hardly visible for  $\Gamma = 0.51$  (figure 13), because the liquid bridge is much shorter and lighter than for the longer bridge with  $\Gamma = 1.66$  (figure 14), because the radius is the same in both cases. Even though the flow for  $\Gamma = 1.66$  is affected much more strongly by the hydrostatic deformation of the liquid bridge and by buoyancy forces for the present parameter variation, all critical modes show the generic structure of axial vortices and internal perturbation temperature extrema of hydrothermal waves. The instability mechanism is qualitatively the same for all modes, and similar arguments hold as for the reference case discussed in § 4.1. In particular, from figure 15, the energy budgets do not change very much with  $\Gamma$ . While there is a visible jump of the energy terms in the liquid at  $\Gamma^{1,3}$ , as expected for a modal change, the jump at  $\Gamma^{3,4}$  is hardly visible. The jump at  $\Gamma^{1,3}$  is related to the particular structure of the  $m = 1$  mode, which admits a flow across the axis of symmetry (cf. table 2) representing a

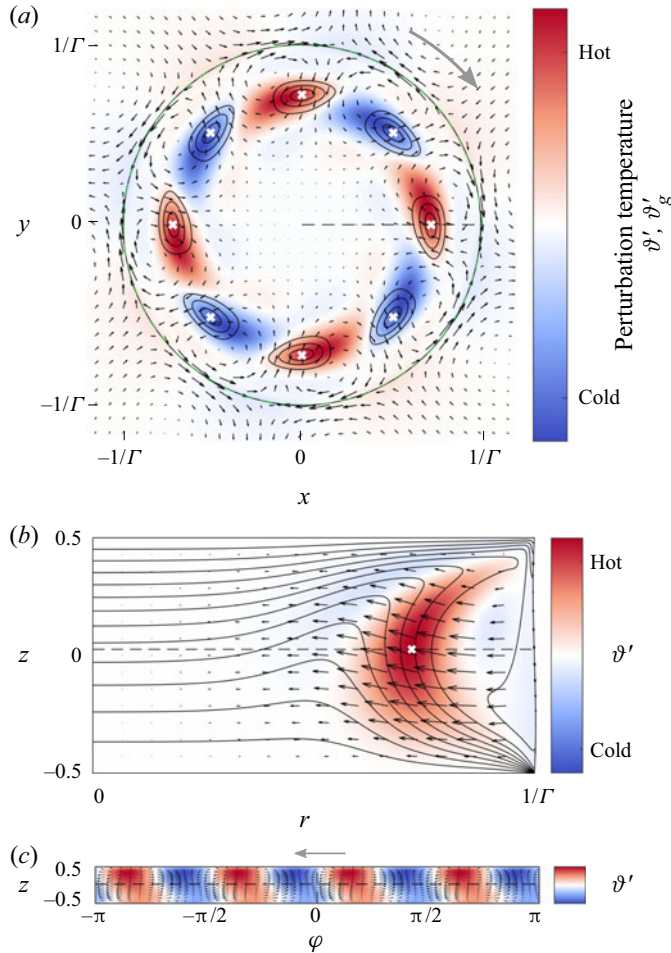


Figure 13. Critical velocity (black arrows) and temperature (colour) fields for  $\Gamma = 0.51$ ,  $Re_c = 597$ ,  $Bd = Bd_{ref} \times (\Gamma/\Gamma_{ref})^2$  and  $m_c = 4$ . (a) Horizontal cross-section at  $z = 0.03$  in which the local thermal production  $\vartheta' \mathbf{u}' \cdot \nabla \vartheta_0$  (isolines) takes its maximum (white crosses) in the bulk. (b) Vertical  $(r, z)$  plane in which the local thermal production  $\vartheta' \mathbf{u}' \cdot \nabla \vartheta_0$  (not shown) takes its maximum (white cross) in the bulk. Lines indicate isotherms of the basic state. (c) Perturbation velocity and temperature fields on the free surface. The grey arrows in (a,c) indicate the direction of propagation of the critical mode. The black dashed lines represent the locations of the corresponding cuts. The green circle in (a) indicates the diameter of the support rods.

qualitative difference compared to all other three-dimensional modes. Due to this property, the role of the radial transport of basic state temperature, hence  $J_1$ , is more important for  $m = 1$  and  $\Gamma > \Gamma^{1,3}$ , associated with a particularly strong stabilising effect by  $J_2$  in the liquid (figure 15a). As  $\Gamma$  increases beyond  $\Gamma^{1,3}$ , the critical Reynolds number reduces drastically due to the geometrical constraint that rules the wavenumber selection, and the stabilising effect of  $J_2$  diminishes. For  $\Gamma > 1.66$  (liquid) and  $\Gamma > 1.24$  (gas), both  $J_1$  and  $J_2$  become positive (not shown).

Also shown in figure 12(a) is a critical Reynolds number (green square) for  $\Gamma = 1$  obtained by Yano *et al.* (2016) for the same volume, and a similar radius ratio and Bond number. Note, however, that the thermal conditions on  $r = \eta/\Gamma$  differ in that Yano *et al.* (2016) have imposed a constant temperature  $T(r = \eta/\Gamma) = 20^\circ\text{C}$  on the outer cylindrical



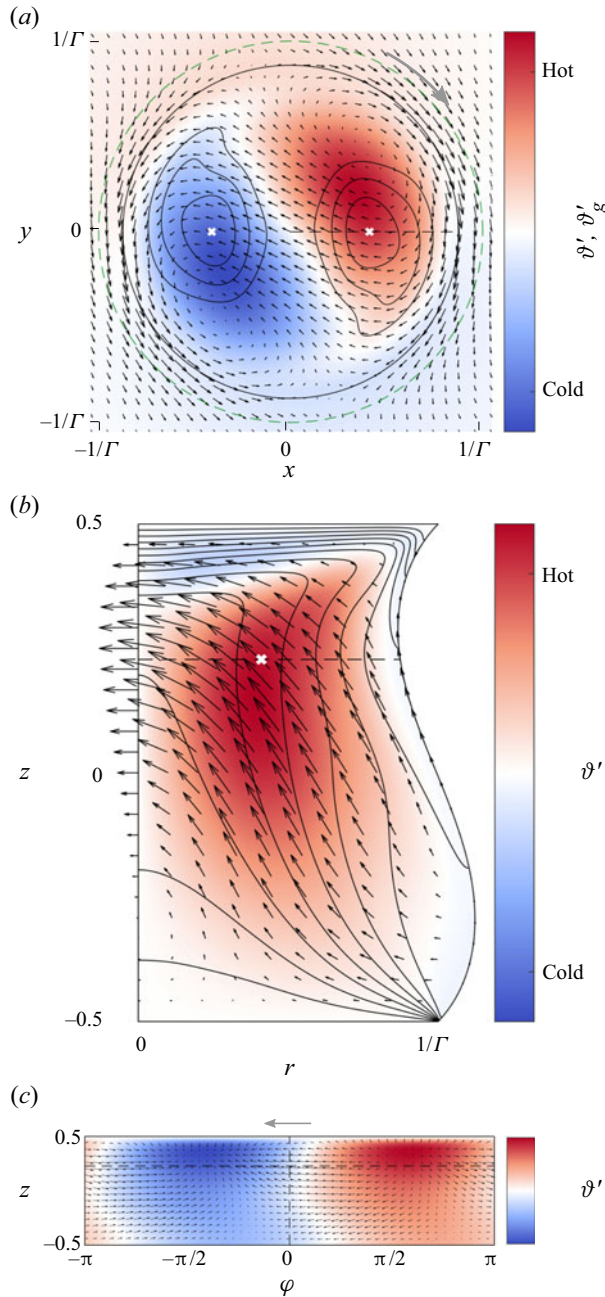


Figure 14. Same as figure 13, but for  $\Gamma = 1.66$ ,  $Re_c = 492$ ,  $Bd = Bd_{ref} \times (\Gamma/\Gamma_{ref})^2$ ,  $m_c = 1$  and  $z = 0.23$ .

wall of the gas container, and fixed  $T_{cold} = 14^\circ\text{C}$ . These conditions lead to a cooling of the liquid bridge from the outer shield as soon as  $T_{hot} \gtrsim 26^\circ\text{C}$ , which is indeed the case in the reported experiments. Also, the aspect ratio  $\Gamma_{rod} = 4.8$  of the support rods in Yano *et al.* (2016) is much larger than the present value  $\Gamma_{rod} = 0.4$ . In view of the importance of the gas phase for the critical Reynolds number (orange and white squares in figure 12, see also Kamotani *et al.* 2003), it is not surprising that  $Re_c$  and  $m_c$  obtained by Yano *et al.*



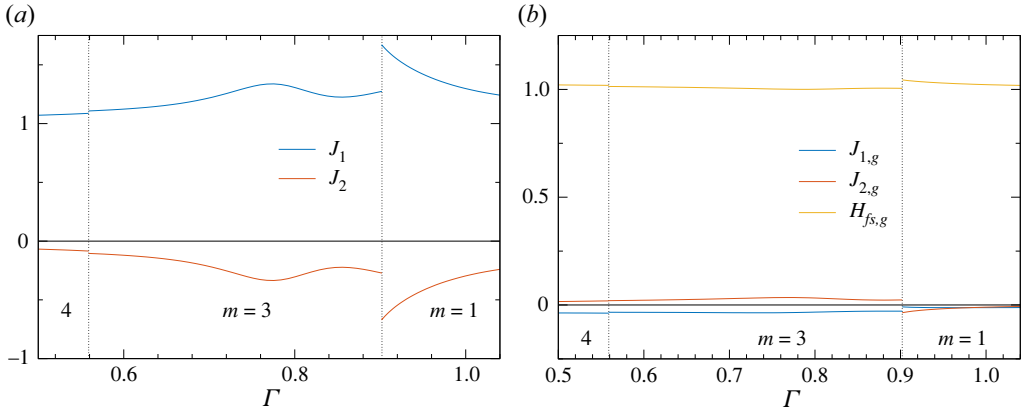


Figure 15. Normalised contributions  $J_1$ ,  $J_2$  and  $H_{fs}$  to the thermal energy budget as functions of  $\Gamma$  for the critical conditions shown in figure 12(a). The vertical dotted lines indicate  $\Gamma^{1,3}$  and  $\Gamma^{3,4}$  where  $m_c$  (indicated by labels) changes. (a) Liquid phase; throughout  $-0.0037 < H_{fs} < 0$ . (b) Gas phase.

(2016) differ from the present critical data. The deviation of the critical Reynolds number obtained by Ueno *et al.* (2010) for  $\Gamma = 0.64$  (bright blue square in figure 12a) from the present data may be due to similar reasons. These comparisons demonstrate the important influence of the geometrical and thermal properties of the gas phase on the critical onset.

The effect on the critical Marangoni number of a partial confinement of the gas phase by partition disks was investigated experimentally by Irikura *et al.* (2005) in a geometry similar to the present one, also using the same working fluids. Since the critical temperature difference was always less than 17 °C, the thermal properties of the gas phase near the onset are comparable to the present ones. However, the geometry was slightly different: in our computations, the gas phase is radially confined by an adiabatic rigid wall, whereas it was open to the ambient in the experiments of Irikura *et al.* (2005). In their experiments, the effective length of the hot support rod was varied by axially moving a partition disk on the rod. For comparison, we adapted our geometry accordingly by selecting  $\Gamma = 1$ ,  $\eta = 6.55$  and  $d_{rod,c} = 1$  mm, and computed the critical Marangoni number as a function of the length  $d_{rod,h}$  of the hot (upper) support rod for the data provided by Irikura *et al.* (2005). The result is shown as a line in figure 16. In qualitative agreement with Irikura *et al.* (2005) (circles in figure 16), we find a reduction of the critical Marangoni number (line) as the length of the hot rod  $d_{rod,h}$  is increased. The systematically larger numerical critical Marangoni numbers are attributed mainly to the different radial boundary conditions: an adiabatic wall in the numerics versus a gas phase open to the ambient atmosphere in the experiment. The coupling of the gas phase to the ambient air in the experiment may have caused mechanical and thermal perturbation, which may explain the scatter of the experimental data.

#### 4.3. Effect of the volume ratio

The influence of the volume ratio  $\mathcal{V}$  on the stability of the basic flow with  $\Gamma_{ref} = 0.66$  and  $Bd_{ref} = 0.41$  is shown in figure 17. The critical curve is made of segments of neutral Reynolds number belonging to all wavenumbers from  $m = 0$  to  $m = 4$ . The critical modes change at the codimension-two points given in table 5. The well-known strong stabilisation of the flow near  $\mathcal{V} = 0.9$  for 2 and 10 cSt silicone oils found by Sakurai *et al.* (1996) and Hu *et al.* (1994), respectively, is confirmed (see also Tang & Hu 1999). We find the maximum stabilisation at  $\mathcal{V}^{0,1} = 0.8917$  with  $Re_c = 2319$ . The experimental critical data of Sakurai

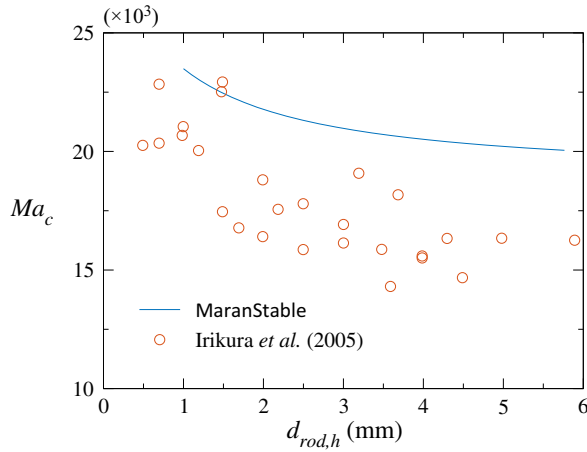


Figure 16. Critical Marangoni number  $Ma_c = Pr Re_c$  ( $m = 1$ , line) as a function of the length  $d_{rod,h}$  of the upper (hot, subscript  $h$ ) supporting rod. The length of the lower (cold, subscript  $c$ ) support rod was kept constant at  $d_{rod,c} = 1$  mm, corresponding to the experiment of Irikura *et al.* (2005) whose data are reproduced as circles. The liquid bridge has length  $d = 2.5$  mm and aspect ratio  $\Gamma = 1$ . The radius ratio  $\eta = 6.55$  is estimated from figure 1 of Irikura *et al.* (2005).

*et al.* (1996) for 2cSt silicone oil, with  $\Gamma = 1$ ,  $Bd = 0.95$  and otherwise uncontrolled ambient conditions, are shown in figure 17 as crosses. They agree qualitatively (despite the deviation in  $\Gamma$  and  $Bd$ ), but differ quantitatively.

Surprisingly, a very small window of the volume ratio exists within which the critical mode is axisymmetric with  $m = 0$ . A similar axisymmetric oscillatory mode near the so-called gap region was found by Xun, Li & Hu (2010) near  $\mathcal{V} \approx 0.8$  by a linear stability analysis, although for a single-fluid model with  $Pr = 68.6$  (5cSt silicone oil) and an adiabatic free surface.

Similarly to before, the contribution to the thermal energy budget is dominated by  $J_1$  (building on radial gradients of  $\vartheta_0$ ) for all critical modes, with  $J_2$  (building on axial gradients of  $\vartheta_0$ ) being small or negative (stabilising; figure 18). This indicates the predominance of axial vorticity in the critical mode, except for the axisymmetric mode. As another observation, the critical wavenumber does not depend monotonically on  $\mathcal{V}$ . Considering the structure of the neutral modes, it is possible to understand qualitatively the non-monotonic dependence of the critical Reynolds number on  $\mathcal{V}$ : for a small volume fraction  $\mathcal{V} = 0.8$  ( $m_c = 2$ ; figure 19), the internal temperature extrema of the hydrothermal wave are located quite close to the free surface. This facilitates the coupling between the temperature and velocity perturbations, because the free-surface temperature spots are more easily created by the internal temperature extrema. Hence the critical Reynolds number is relatively small for small  $\mathcal{V}$ . As  $\mathcal{V}$  increases, the internal temperature extrema must be stronger to be able to heat/cool the more distant free surface and to generate the perturbation flow ( $\mathcal{V} = 0.87$ ,  $m_c = 1$ ; figure 20). This may explain the increase of the critical Reynolds number with  $\mathcal{V}$  before reaching its maximum. However, as the volume gets very large ( $\mathcal{V} = 1.3$ ,  $m_c = 3$ ; figure 21), the basic flow and the perturbation flow suffer less viscous dissipation, because the liquid volume is bounded mainly by a free surface, only coupled to the gas phase. As a result, the critical Reynolds number decreases again after  $\mathcal{V}$  has exceeded the point of maximum stabilisation (for  $\mathcal{V} > 0.8917$ ).

Near the volume ratio  $\mathcal{V} > 0.8917$  at which the maximum stabilisation is observed, a small window arises in which the critical mode is axisymmetric. Contrary to the other

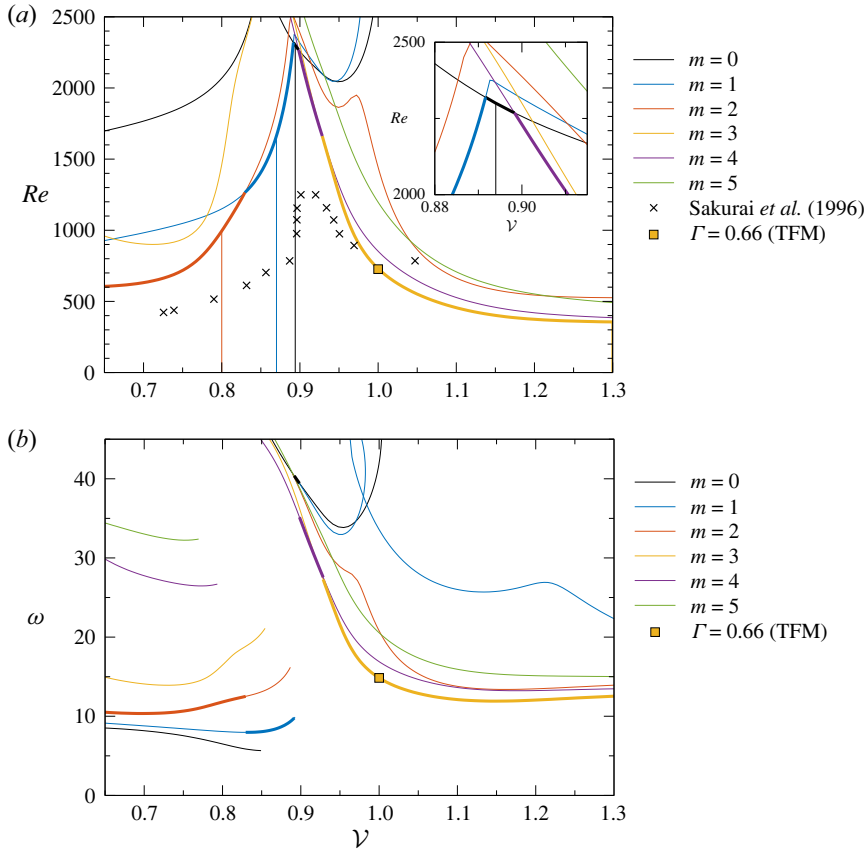


Figure 17. (a) Neutral Reynolds numbers (thin lines) and critical Reynolds numbers  $Re_c$  (thick lines) as functions of the volume ratio  $\mathcal{V}$  for  $\Gamma = 0.66$  and  $Bd = 0.41$ . Crosses indicate data taken from Sakurai *et al.* (1996) for  $\Gamma = 1$  and  $Bd = 0.95$ . (b) Corresponding frequencies  $\omega$ . The yellow square indicates the reference case.

$m$	$1 \leftrightarrow 2$	$0 \leftrightarrow 1$	$0 \leftrightarrow 4$	$3 \leftrightarrow 4$
$\mathcal{V}^{m_1, m_2}$	0.8296	0.8917	0.8983	0.9286
$Re_c(\mathcal{V}^{m_1, m_2})$	1264	2319	2268	1662

Table 5. Codimension-two points where critical curves for constant  $m$  intersect, with  $\Gamma = 0.66$ ,  $Bd = 0.41$ .

modes, the axisymmetric mode  $m_c = 0$  draws its thermal energy from both axial and radial temperature gradients, with both  $J_1$  and  $J_2$  being positive (figure 18). The mode arises as a toroidal vortex ( $\mathcal{V} = 0.8939$ ; figure 22) whose sense of rotation oscillates with  $\omega_c(m = 0)$ . The total nonlinear flow in an experiment would thus appear as a toroidal vortex whose strength, position and size change periodically in time.

#### 4.4. Effect of buoyancy

The linear stability boundary and oscillation frequency as functions of the dynamic Bond number for  $\Gamma_{ref} = 0.66$  and  $\mathcal{V}_{ref} = 1$  are displayed in figure 23 for heating from above

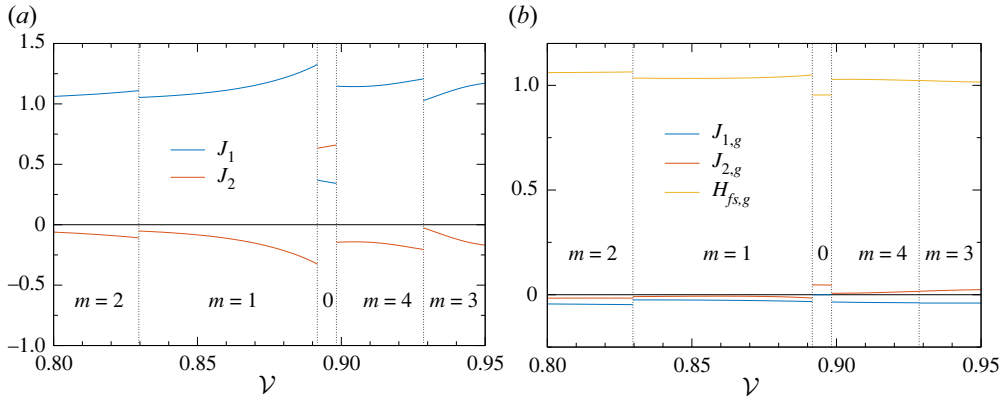


Figure 18. Normalised contributions  $J_1$ ,  $J_2$  and  $H_{fs}$  to the thermal energy budget as functions of  $\mathcal{V}$  along the critical curve shown in figure 17(a). The vertical dotted lines indicate  $\mathcal{V}^{1,2}$ ,  $\mathcal{V}^{0,1}$ ,  $\mathcal{V}^{0,4}$  and  $\mathcal{V}^{3,4}$  at which  $m_c$  (indicated by labels) changes. (a) Liquid phase; throughout  $-0.007 < H_{fs} < 0$ . (b) Gas phase.

( $Bd > 0$ ) and heating from below ( $Bd < 0$ ). The crossover points at which the wavenumber of the critical mode changes are listed in table 6. It should be noted that a quiescent liquid bridge of  $\Gamma = 0.66$  and  $\mathcal{V} = 1$  would break mechanically due to the capillary instability at  $Bo = \pm 31.75$  (Slobozhanin & Perales 1993). For the present working fluid, this limit corresponds to  $Bd = \pm 10.31$ . Therefore, the range shown in figure 17 is safely within the mechanical stability limits of the liquid bridge, even if dynamic surface deformations were taken into account.

In the range  $-0.25 \lesssim Bd \lesssim 0.35$ , buoyancy has only a small effect on the shape of the liquid bridge and on the magnitude of the critical Reynolds number. Since the governing equations are not invariant under  $Bd \rightarrow -Bd$ , the slope of the critical curve at zero gravity ( $Bd = 0$ ) does not vanish. This was also found by Wanschura *et al.* (1997b) for small values of  $Bd$  and a cylindrical liquid bridge with  $Pr = 4$ ,  $\Gamma = 1$  and an adiabatic free surface. For weak stabilising buoyancy and  $Bd > Bd^{2,3}$ , the critical mode has  $m_c = 3$  (yellow), whereas for  $Bd < Bd^{2,3}$  and for destabilising buoyancy, the critical wavenumber is  $m_c = 2$  (red). The Bond numbers corresponding to the gravity levels on the Moon, Mars and Earth are indicated by yellow vertical dashed lines. For zero gravity conditions, the critical mode with  $m_c = 2$  is illustrated in figure 24. The basic flow in an upright cylindrical liquid bridge, exclusively driven by thermocapillarity, is a standard case within the single-fluid model. Here, however, the flow is modified by the presence of the ambient gas phase. The properties of the hydrothermal wave are similar to those discussed in § 4.1.2 for the reference case, which differs by the Bond number.

As the Bond number is increased beyond  $Bd > 0.41$  (Earth gravity level), the critical Reynolds number increases significantly. This seems to be consistent with a more stable density stratification as  $Bd$  increases. However, for  $Bd > Bd^{1,5} \approx 0.91$ , the critical Reynolds number decreases again, mainly due to an  $m = 2$  mode. A possible explanation is that the hot fluid transported downward along the free surface by the thermocapillary surface flow has a strong tendency to rise in the bulk, owing to its buoyancy. As a result, the basic thermocapillary-driven vortex has little radial extent, and the internal temperature gradients, which provide the source of the thermal perturbation energy, arise in the close vicinity of the free surface. This can be seen in figure 25, which shows the critical mode for  $Bd = 1.1$ . Since the thermocapillary flow does not penetrate very much inwards from

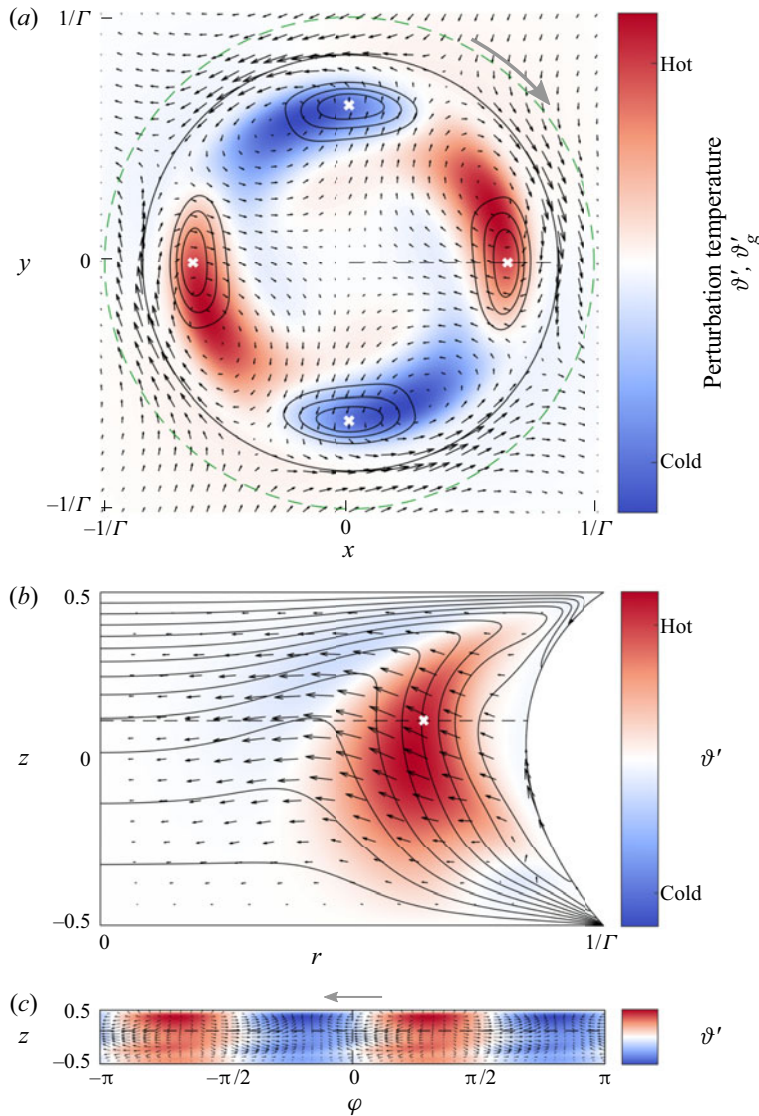


Figure 19. Same as figure 13, but for  $\Gamma = 0.66$ ,  $\mathcal{V} = 0.8$ ,  $Re_c = 995$ ,  $m_c = 2$  and  $z = 0.12$ .

the free surface, the free-surface temperature perturbations of the critical mode are much easier to create as compared to lower Bond numbers, in particular as compared to  $Bd \approx 0$  (figure 24). This facilitates the coupling between temperature and velocity perturbations, and leads to a reduction of the critical Reynolds number despite the nominally stabilising buoyancy forces.

The critical mode for  $Bd = 1.1$  is also affected by buoyancy. To analyse this effect, we separate the buoyancy effect on the critical mode from the buoyancy effect on the basic flow, by using the same basic state solution ( $Bd = 1.1$ ), but artificially setting  $Bd \equiv 0$  in the perturbation equations. Compared to figure 25, the spatial structure of the perturbation temperature  $\vartheta'$  remains similar, while the vertical perturbation velocity is very small everywhere ( $w' \approx 0$ ), except close to the free surface (not shown). Due to the nearly



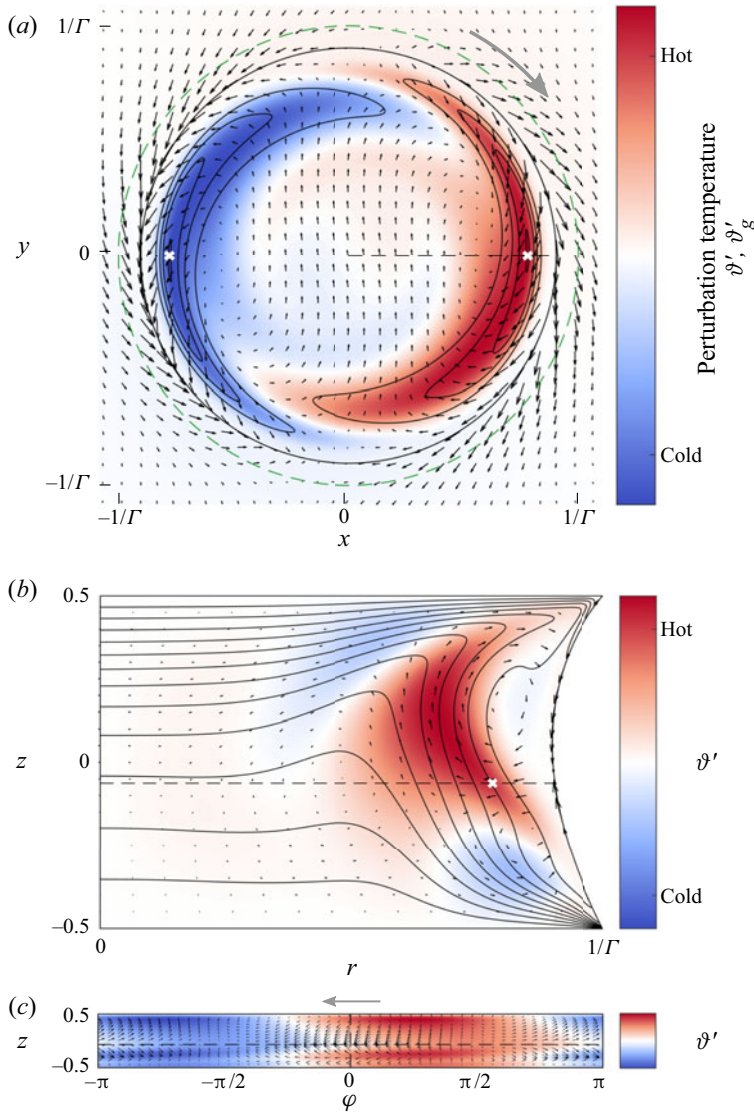


Figure 20. Same as figure 13, but for  $\Gamma = 0.66$ ,  $\mathcal{V} = 0.87$ ,  $Re_c = 1664$ ,  $m_c = 1$  and  $z = -0.06$ .

horizontal velocity perturbation in the bulk (axial vorticity), more thermal perturbation energy is generated, which would destabilise the basic state. This means that for  $Bd = 1.1$ , the action of buoyancy in the perturbation flow has a stabilising effect on the basic state. Therefore, the destabilising trend for increasing Bond number for  $Bd > Bd^{1.5} = 0.9083$  is caused by the facilitated feedback between internal and surface temperature extrema due to the structure of the basic flow, and not by the action of buoyancy on the perturbation flow.

Contrary to what one would expect for destabilising buoyancy (heating from below,  $Bd < 0$ ) the critical Reynolds number also increases as  $Bd$  is decreased. This effect is related to a similar mechanism as discussed before: the hot fluid that is transported to the cold wall along the free surface has little tendency to return to the hot wall in the bulk due



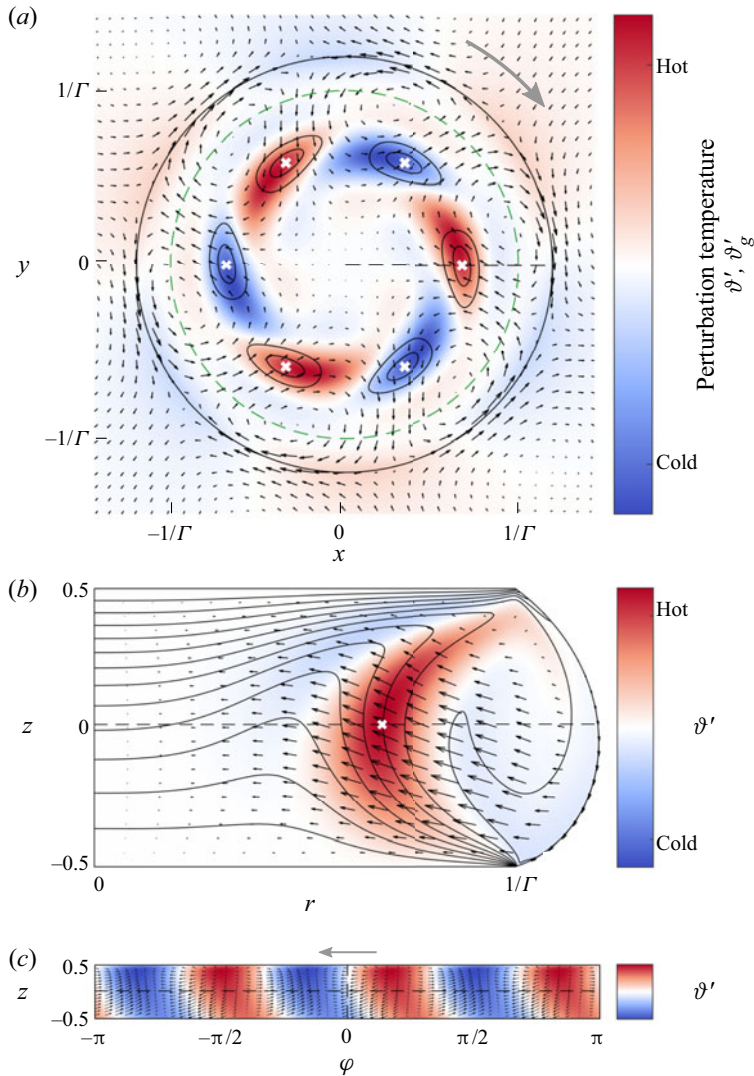


Figure 21. Same as [figure 13](#), but for  $\Gamma = 0.66$ ,  $\mathcal{V} = 1.3$ ,  $Re_c = 356$ ,  $m_c = 3$  and  $z = 0.01$ .

to buoyancy. As a result, the thermocapillary basic state vortex (not shown) has a larger radial extension and the energy source for the hydrothermal wave arises closer to the axis of the liquid bridge. Therefore, the internal perturbation temperature extrema cannot easily heat/cool the distant free surface to drive the velocity field necessary for the hydrothermal wave feedback mechanism. As a result,  $Re_c$  increases.

The black dotted curve in [figure 23\(a\)](#) indicates a Rayleigh number  $Ra = 1700$ , where  $Ra = -Pr B d Re$  is defined in agreement with the usual convention for pure buoyancy-driven flows. This is roughly the Rayleigh number at which the flow becomes buoyantly unstable in a cylindrical adiabatic liquid bridge in the absence of thermocapillarity (Wanschura, Kuhlmann & Rath 1996). To the left of it, destabilising buoyancy forces get even stronger. However, pure buoyant instabilities are absent here, mainly because the basic thermocapillary flow significantly deforms the basic temperature field that would be conducting in the absence of thermocapillarity. Nevertheless,

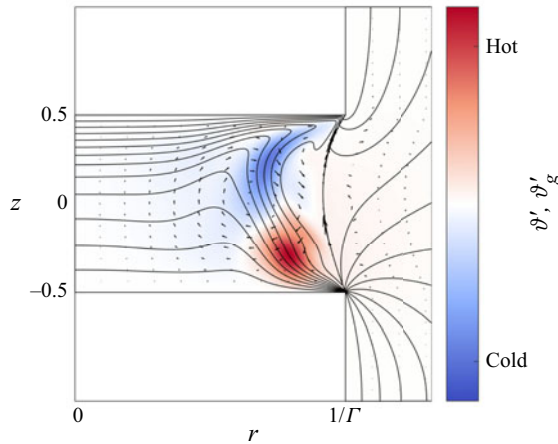


Figure 22. Axisymmetric critical mode for  $\mathcal{V} = 0.8939$ ,  $Re_c = 2301$  and  $m_c = 0$ . Shown are the basic state isotherms (lines), the critical velocity field (arrows) and the critical temperature field (colour).

destabilising buoyancy is expected to promote the instability of the basic flow for decreasing  $Bd$ . Such destabilisation is not seen, however, until  $Bd = Bd^{1,2}$ .

Only for  $Bd < Bd^{1,2} = -0.5645$ , a critical mode with  $m_c = 1$  (blue) arises that seems to be affected by destabilising buoyancy. The critical mode for  $Bd = -1.25 < Bd^{1,2}$  is shown in figure 26. At a first inspection of figures 26(a,c), the critical mode seems to be driven by an azimuthal thermocapillary effect. The associated radial flow in the bulk crosses the axis and creates a cold spot and a hot spot very close to the axis, since this is the region of largest radial gradients of the basic temperature field. However, in the absence of the action of buoyancy on the perturbation flow, there would be no obvious reason why the perturbation flow should not be essentially horizontal near the axis, as for  $Bd = 0$  (figure 24b). Instead, we find a strong vertical upward (downward) flow near the hot (cold) near-axis perturbation temperature spots. This leads to a localised convection role in the plane of maximum thermal energy production shown in figure 26(b). Artificially switching off the Bond number in the perturbation equation only (setting  $Bd \equiv 0$ ), while keeping  $Bd = -1.25$  for the basic state, reveals (not shown) that the perturbation flow in this artificial case is indeed horizontal near the axis. Thus the vertical component of the velocity of the perturbation vortex near the axis must be driven essentially by buoyancy acting on the perturbation mode. The buoyancy effect on the perturbation mode should be particularly high in this case, because the horizontal temperature gradient of the perturbation flow (generated by the thermocapillary return flow) is particularly large when the perturbation temperature spots arise over a very small distance close to the axis.

This interpretation is confirmed by inspecting the major terms of the kinetic energy budget. These terms, corresponding to the work per time driving the perturbation flow, are given in table 7. Compared to  $Bd = 0.41$ , the work done by buoyant forces in case of  $Bd = -1.25$  is more than ten times as large and amounts to approximately 14 % of the total kinetic energy production. But the major driving of the perturbation flow field is still caused by the work done by thermocapillary forces  $M_z$  and  $M_\phi$ . Among these, the production  $M_z$  due to axial thermocapillary stresses for  $Bd = -1.25$  is surprisingly more important than the azimuthal production. This might be related to the strong vertical component of the perturbation flow near the axis.

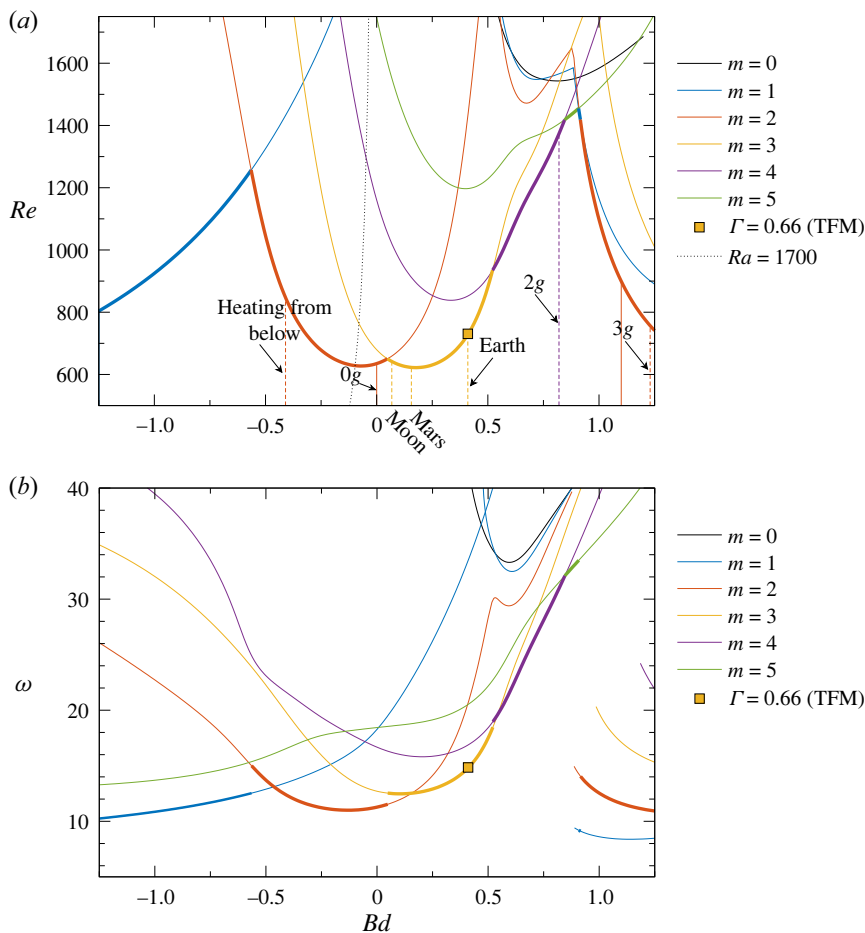


Figure 23. (a) Neutral Reynolds numbers (thin lines) and critical Reynolds numbers  $Re_c$  (thick lines) as functions of the dynamic Bond number  $Bd$  for  $\Gamma_{ref} = 0.66$  and  $\mathcal{V}_{ref} = 1$ . (b) Corresponding neutral and critical frequencies  $\omega$ .

$m$	1 $\leftrightarrow$ 2	2 $\leftrightarrow$ 3	3 $\leftrightarrow$ 4	4 $\leftrightarrow$ 5	1 $\leftrightarrow$ 5	1 $\leftrightarrow$ 2
$Bd^{m_1, m_2}$	-0.5645	0.0483	0.5214	0.8457	0.9083	0.9162
$Re_c(Bd^{m_1, m_2})$	1257	650	935	1420	1455	1419

Table 6. Codimension-two points where critical curves for constant  $m$  intersect, with  $\Gamma_{ref} = 0.66$ ,  $\mathcal{V}_{ref} = 1$ .

The thermal energy budget as function of the Bond number is shown in figure 27. As in the previous cases, the thermal energy per time  $H_{fs,g}$  supplied to the gas phase through the interface is essentially dissipated, with the thermal energy production rates  $J_{1,g}$  and  $J_{2,g}$  being insignificant. Therefore, the instability is always triggered in the liquid phase. While for  $Bd < Bd^{2,3} \approx 0.05$  both  $J_1$  and  $J_2$  are positive and contribute to the destabilisation of the basic flow,  $J_2$  is negative for  $Bd > Bd^{2,3}$ , which, on the stability boundary, is compensated by a much larger positive value of  $J_1$ . This indicates the dominant role for the instability of radial temperature gradients of the basic state when the liquid bridge

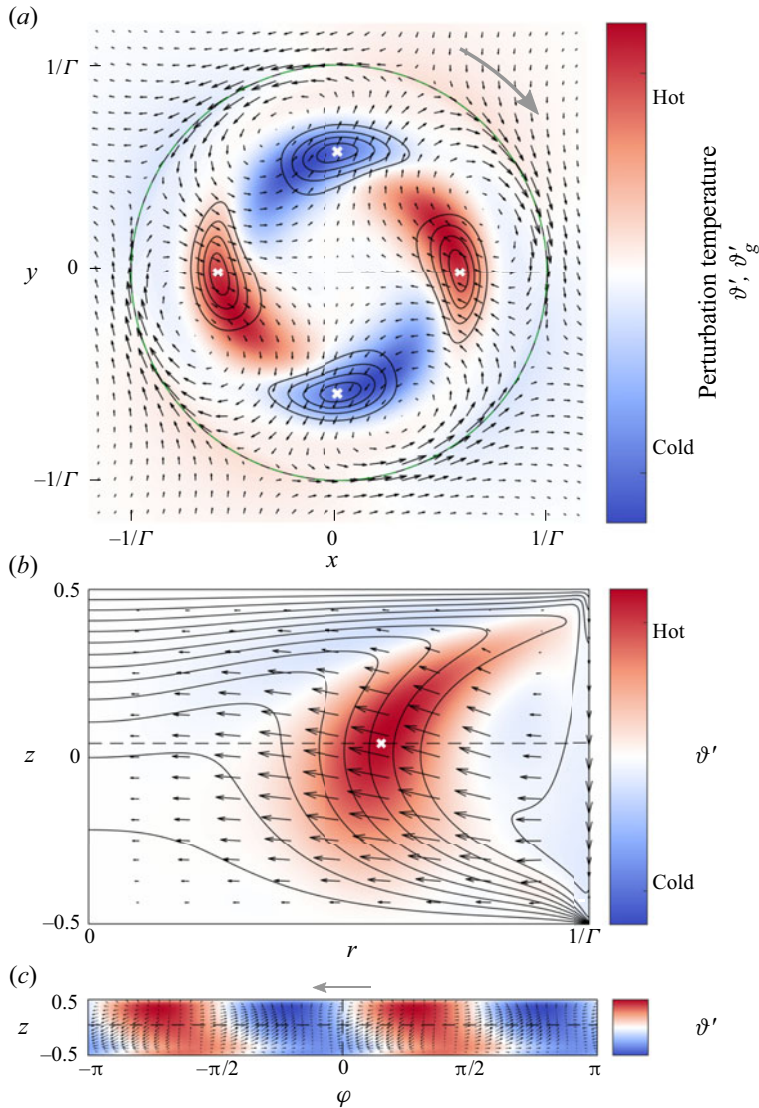


Figure 24. Same as figure 13, but for  $\Gamma = 0.66$ ,  $Bd = 0$ ,  $Re_c = 635$ ,  $m_c = 2$  and  $z = 0.04$ .

is heated from above (buoyancy forces are opposing basic state thermocapillarity forces on the free surface,  $Bd > 0$ ), consistent with the above-described small radial penetration depth of the basic flow when buoyancy forces are large. For heating from below (buoyancy forces are augmenting the basic state thermocapillarity forces on the free surface,  $Bd < 0$ ), the perturbation flow can also extract thermal energy from the axial gradients of the basic temperature field via  $J_2 > 0$ , albeit radial temperature gradients of the basic state remain more important.

For heating from below and in the absence of thermocapillary effects, Wanschura *et al.* (1996) found that the onset of thermal convection in cylindrical liquid bridges is always non-axisymmetric. Nevertheless, steady axisymmetric solutions exist for Rayleigh numbers  $Ra = g\beta\Delta Td^3/\nu\kappa$  larger than the neutral stability boundary for  $m = 0$ . These axisymmetric flows have either up- or down-flow at the free surface. Thermocapillary

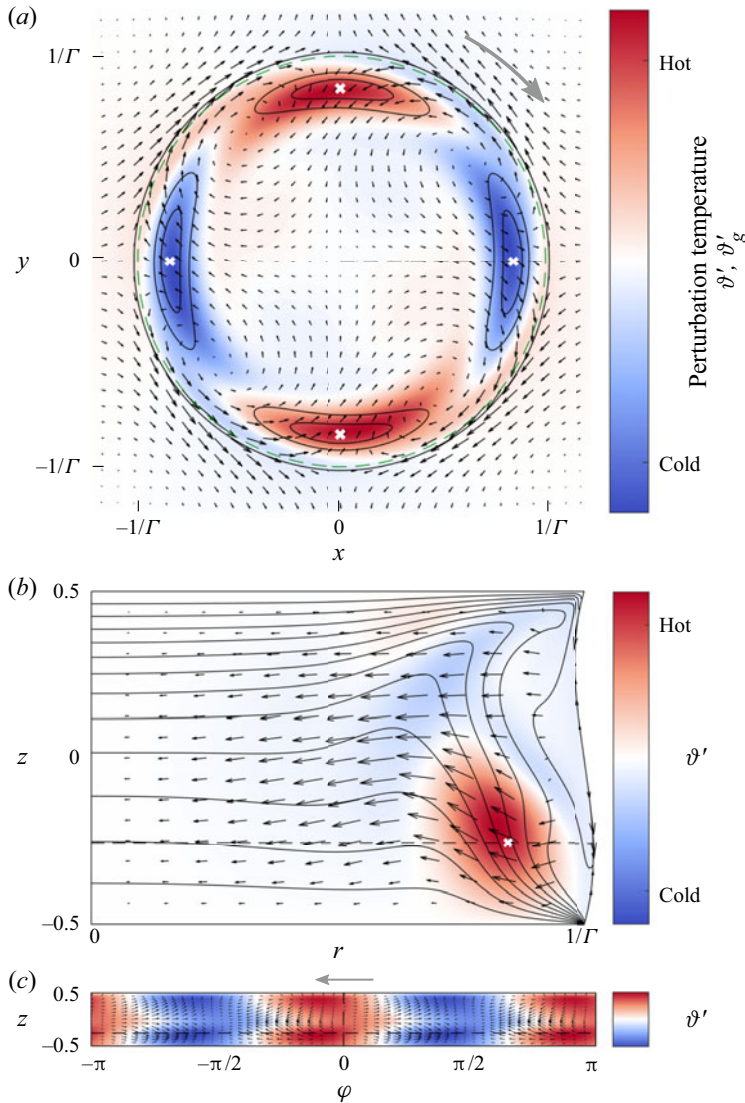


Figure 25. Same as figure 13, but for  $\Gamma = 0.66$ ,  $Bd = 1.1$ ,  $Re_c = 900$ ,  $m_c = 2$  and  $z = -0.26$ .

forces can either augment or oppose the buoyant flow on the free surface. To illustrate the resulting buoyant-thermocapillary flows, the coefficient  $\gamma = -3.828 \times 10^{-7} \text{ N m}^{-1} \text{ K}^{-1}$  is selected small due to e.g. impurities or surfactants dissolved in the liquid. For  $\Gamma = 0.66$ ,  $\mathcal{V} = 1$ ,  $Ra = 3200$ ,  $Re = 0.5$  and  $Bd = -229$ , the augmenting and opposing axisymmetric flows are illustrated in figures 28(a) and 28(b), respectively. For the opposing case (figure 28b), the direction of the surface flow is reversed near each of the two triple-phase contact lines such that a small eddy arises in the hot as well as in the cold corner. In addition to these two states, an intermediate weak state exists (figure 28c) in which the velocity field near the liquid–gas interface is very weak and which is unstable with respect to two-dimensional perturbations. This result is similar to the behaviour in adiabatic cylindrical liquid bridges using the single-fluid model (Wanschura *et al.* 1997b). We find that the flow in the augmenting case (strong solution; figure 28a) is linearly stable



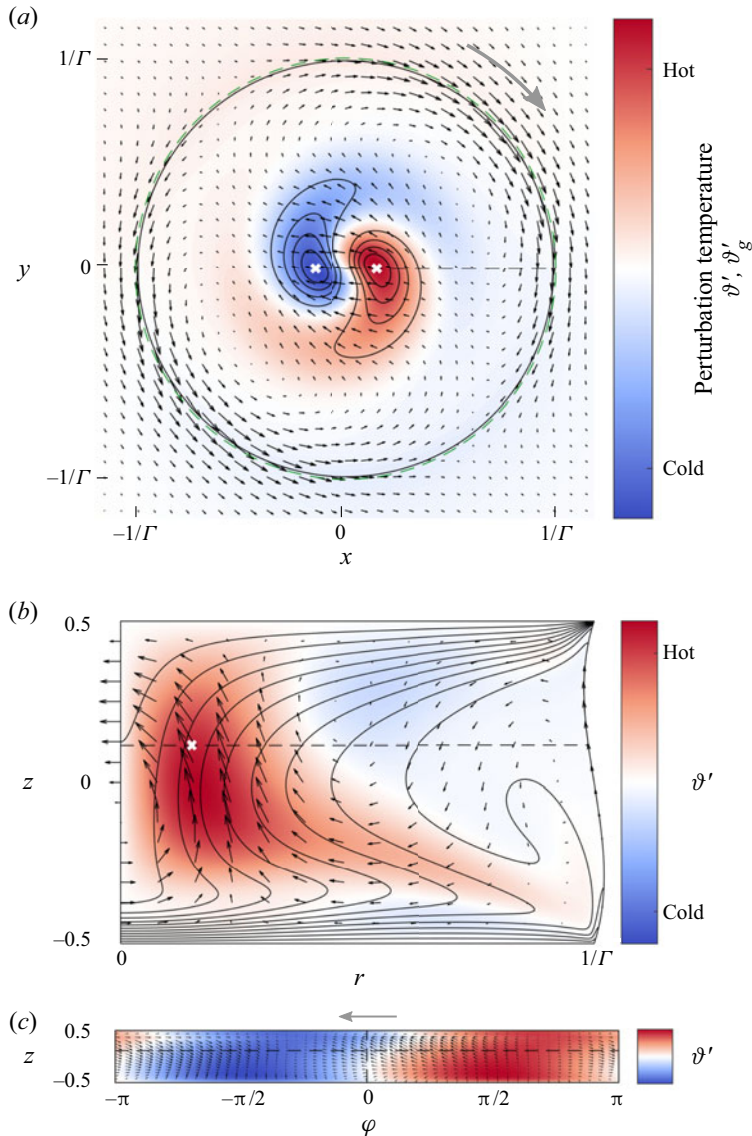


Figure 26. Same as figure 13, but for  $\Gamma = 0.66$ ,  $Bd = -1.25$ ,  $Re_c = 804$ ,  $m_c = 1$  and  $z = 0.12$ . Note that for  $Bd < 0$ , the hot wall is located at the bottom (heated from below).

with respect to all modes, with  $m \in [0, 5]$ , the most dangerous mode having  $m = 3$  and a growth rate  $\mu = -0.03 + 0i$ . The flow in the opposing case (weak solution; figure 28b) is stable with respect to  $m \in [0, 2]$ , but unstable for  $m \in [3, 5]$ , with the most dangerous mode  $m = 4$  and  $\mu = 0.15 + 0i$ . Finally, the third weak state (figure 28c) is unstable to all modes with  $m \in [0, 5]$ , the most dangerous having the wavenumber  $m = 4$  with  $\mu = 0.53 + 0i$ .

## 5. Discussion and conclusions

The linear stability of axisymmetric steady flow in liquid bridges of silicone oil with  $Pr = 28$  in air has been investigated numerically. This pair of fluids is used also in



$Bd$	$M_r$	$M_\varphi$	$M_z$	$B$
+0.41	0.002	0.531	0.481	0.013
-1.25	0.040	0.185	0.521	0.142

Table 7. Main contributions to the kinetic energy production at the critical point for  $\Gamma_{ref} = 0.66$  and  $\mathcal{V}_{ref} = 1$ .

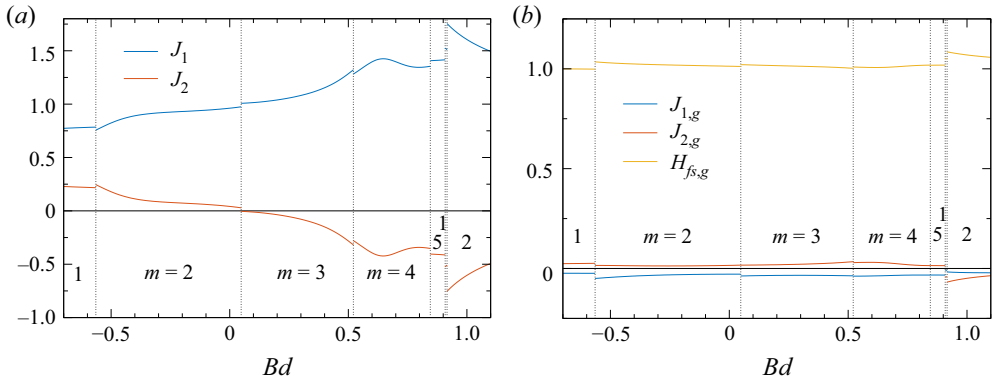


Figure 27. Normalised contributions  $J_1$ ,  $J_2$  and  $H_{fs}$  to the thermal energy budget at criticality (figure 23a) as functions of  $Bd$  for  $\Gamma_{ref} = 0.66$  and  $\mathcal{V}_{ref} = 1$ . The vertical dotted lines indicate  $Bd^{1,2}$ ,  $Bd^{2,3}$ ,  $Bd^{3,4}$ ,  $Bd^{4,5}$ ,  $Bd^{1,5}$  and  $Bd^{1,2}$  where  $m_c$  (indicated by labels) changes. (a) Liquid phase; throughout  $-0.0035 < H_{fs} < 0$ . (b) Gas phase.

many experimental investigations (see e.g. Ueno *et al.* 2003; Irikura *et al.* 2005; Tanaka *et al.* 2006; Yano, Hirotsu & Nishino 2018a). While taking into account the hydrostatic deformation of the liquid bridge, the liquid and gas flows are treated in Boussinesq approximation in order to reduce the large parameter space. Furthermore, the radii of the support cylinders and the cylindrical gas container relative to the radius of the liquid bridge were kept fixed. This set-up allowed us to investigate the effects of the relative length of the liquid bridge ( $\Gamma$ ), the relative volume of liquid ( $\mathcal{V}$ ), and buoyancy forces ( $Bd$ ) on the threshold for the onset of three-dimensional flow. The linear stability boundary of the basic axisymmetric flow was calculated quasi-continuously varying these three parameters. All parameter variations originated from a common reference case, defined by  $\Gamma_{ref} = 0.66$ ,  $\mathcal{V}_{ref} = 1$  and  $Bd_{ref} = 0.41$ .

Throughout the range of parameters considered, the flow becomes unstable to hydrothermal waves, except for sufficiently strong heating from below when the critical mode arises as a convection roll in the centre of the liquid bridge. Quite generally, the hydrothermal waves exhibit  $2m$  strong azimuthally periodic temperature extrema in the bulk of the liquid. As expected for hydrothermal waves, inertia effects are insignificant for the critical mode, which can hardly extract momentum from the basic vortex flow. On the other hand, advection of basic state temperature by the weak perturbation flow is of key importance for the creation of the characteristic internal temperature extrema. Considering the thermal energy budget of the critical mode, and its spatial structure, allowed us to understand the global trends of the critical Reynolds number  $Re_c$ .

The critical wavenumber  $m$  is found to depend on  $\Gamma$ ,  $\mathcal{V}$  and  $Bd$ . Within the parameter space considered, the critical wavenumber cannot be predicted based on a simple

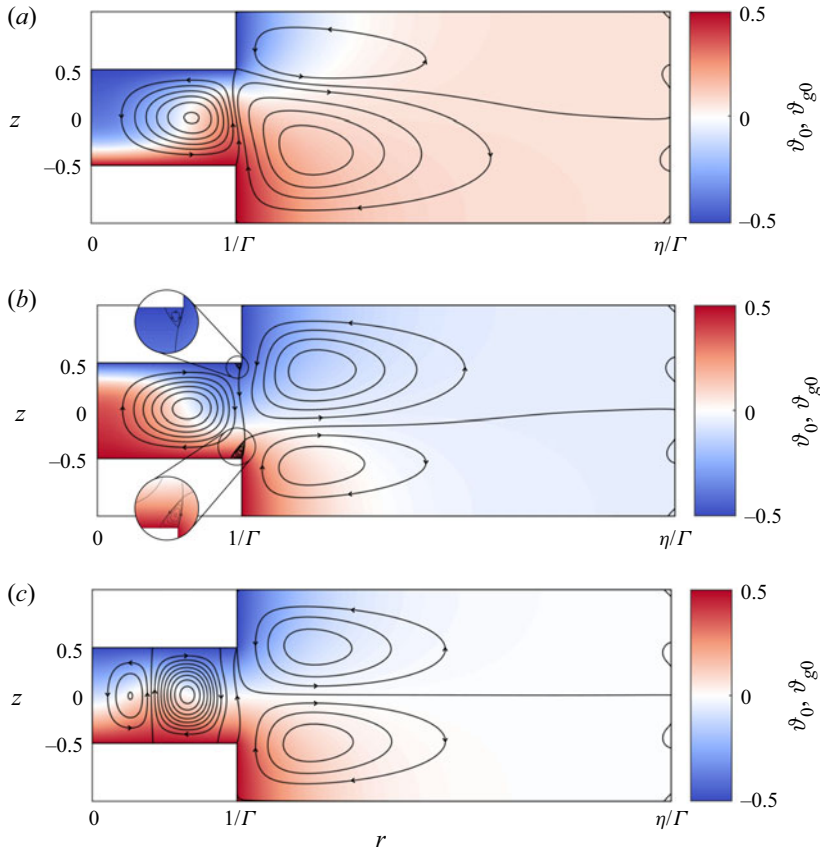


Figure 28. Three different axisymmetric flows for  $\Gamma = 0.66$ ,  $\mathcal{V} = 1$ ,  $Ra = 3200$ ,  $Re = 0.5$  and  $Bd = -229$ . (a) Thermocapillarity is augmenting the buoyant flow. (b,c) Thermocapillarity is opposing the buoyant flow with the strong state shown in (b) and the weak state shown in (c).

correlation like  $m_c \approx 2.2 \times \Gamma$  proposed by Preisser *et al.* (1983) for the instability in  $\text{NaNO}_3$  ( $Pr \approx 7$ ), normal gravity and  $\mathcal{V} \approx 1$ , because the Preisser *et al.* (1983) correlation does not include the gravity level and the volume fraction of the liquid. For  $Pr = 28$  and including the surrounding air in the analysis, we find that the critical wavenumber increases with decreasing  $\Gamma$  (for  $\mathcal{V} = 1$  and  $Bd = 0.41 \times (\Gamma/\Gamma_{ref})^2$ ), but misses out  $m_c = 2$ . The dependence of  $m_c$  on  $\mathcal{V}$  does not exhibit any monotonic trend, while the critical wavenumbers are well ordered from  $m_c = 1$  to  $m_c = 5$  when the Bond number is increased from  $Bd = -1.25$  (heating from below) to  $Bd = 0.9083$  (heating from above). Interestingly, we find an axisymmetric oscillatory instability ( $m = 0$ ) for  $\Gamma = 0.66$  and  $Bd = 0.41$  within a small window of  $\mathcal{V} \in [0.8917, 0.8983]$  where the basic flow is extremely stable with a critical Reynolds number of approximately  $Re_c \approx 2300$ .

As a major result, the gas phase has a strong effect on the stability boundary. For instance, the critical Reynolds number taking into account the gas phase can be less than one-half of the critical Reynolds number for a single-fluid model with a passive adiabatic interface (cf. figures 12a and 29). This effect is caused primarily by the change of the thermal environment of the liquid bridge, i.e. by the heat exchange characteristics between the liquid and the gas. The gas phase, however, does not play an active role for the

instability, because neither mechanical nor thermal perturbation energy is produced from the velocity or temperature gradients of the basic state in the gas phase.

Since the Prandtl number of the liquid is quite large, the basic flow exhibits pronounced thermal boundary layers. The scalings of the boundary layer thicknesses on the cold and hot walls that we find in our numerical calculations for the reference case ( $\Gamma_{ref} = 0.66$ ,  $\mathcal{V}_{ref} = 1$ ,  $Bd_{ref} = 0.41$ ) are in excellent agreement with theoretical scalings predicted for a contact angle  $\alpha = 90^\circ$  and the single-fluid model. This finding is particularly notable for two reasons. First, in the presence of gravity, the hydrostatic free surface exhibits a contact angle  $\alpha = 84^\circ$  for the reference case. Second, in our model the liquid bridge is surrounded by a gaseous phase, which was excluded in the theoretical investigations.

The mathematical model employed (Oberbeck–Boussinesq approximation) is based on the assumption of constant thermophysical properties of the fluids, evaluated at  $T_0 = 25^\circ\text{C}$ , except for  $\rho$ ,  $\rho_g$  and  $\sigma$ , which are linearised around  $T_0$ . Despite the relatively moderate critical temperature differences  $\Delta T_c$  found throughout our numerical investigation, the peak values reach  $\Delta T_c \approx 36^\circ\text{C}$ ,  $70^\circ\text{C}$  and  $44^\circ\text{C}$  when varying  $\Gamma$ ,  $\mathcal{V}$  and  $Bd$ , respectively. Additional preliminary computations taking into account the full temperature dependence of all thermophysical properties of the fluids indicate that the temperature dependence can become important near sharp peaks of the critical curve, because it can suffer a certain shift with respect to the parameters varied ( $\Gamma$ ,  $\mathcal{V}$  or  $Bd$ ). But the linear stability boundaries computed for  $\mathcal{V} \geq 1.05$  using temperature-dependent fluid properties deviate only less than 1 % from the present results. Taking into account temperature-dependent fluid properties affects the linear stability boundary in a non-trivial way. Therefore, it deserves a comprehensive analysis that is beyond the scope of this paper. A dedicated study of the linear stability analysis for a multiphase liquid bridge with variable fluids properties is currently underway and will be reported in the future.

The 2cSt silicone oil used in our study has a pour point below  $-120^\circ\text{C}$  and boiling temperature  $88^\circ\text{C}$  (Shin-Etsu 2004). All critical temperatures found in the present investigation go into this range. For  $\Delta T$  close to the highest critical values computed ( $\Delta T_c \approx 70^\circ\text{C}$ ), evaporation, which is not included in our model, may play a significant role. In fact, Simic-Stefani, Kawaji & Yoda (2006) found a strong stabilising effect due to evaporation using the highly volatile liquid acetone ( $Pr = 4.3$ ). On the other hand, Yano *et al.* (2016) claim that the effect of evaporation for the 2cSt silicone oil is negligible for typical critical temperature differences found in their experiments. Their statement is confirmed by figure 31, as our estimate of the linear stability boundary is in agreement with their experimental data. Nevertheless, the numerical model would benefit by including the mass exchange between the liquid and gas phases, in particular, for large critical temperature differences.

An experimental measurement of the critical Reynolds number for thermocapillary liquid bridges is usually quite error-prone due to the small size of the bridge in terrestrial laboratories, possible chemical contaminations of the interface, and the difficulty to control accurately the thermal environment. The current results provide accurate numerical stability data ( $Re_c$ ,  $m_c$ ,  $\omega_c$ ) for a particular geometrical setting, and the dependence of these data on the important control parameters  $\Gamma$ ,  $\mathcal{V}$  and  $Bd$ . Since the critical onset is affected by the gas phase due mainly to the amount and structure of the heat transfer through the liquid–gas interface, a variation of the relative geometry of the axisymmetric gas space (radius, height) is expected to have only a minor influence on the critical data as long as the heat transfer characteristics are not much affected. This can be expected, for example, if only the radius is increased from the current value. If, however, the heat transfer between the liquid and the gas phase is changed – e.g. by a forced axial gas flow

with a given temperature (Gaponenko *et al.* 2021), or by natural convection in a cold gas (Kamotani *et al.* 2003) – then the critical Reynolds number can be modified strongly. While the control of the critical onset by an imposed gas flow is the objective of ongoing work in the framework of the JEREMI project (Shevtsova *et al.* 2014), a systematic study of the effect of the temperature contrast between the liquid bridge and the gas environment would be an interesting problem for future investigations.

**Funding.** This work has been supported by the Austrian Research Promotion Agency (FFG) in the framework of the ASAP14 programme under contract no. 866027.

**Declaration of interests.** The authors report no conflict of interest.

#### Author ORCIDs.

 Mario Stojanović <https://orcid.org/0000-0003-0072-8563>;

 Francesco Romanò <https://orcid.org/0000-0002-9511-4718>;

 Hendrik C. Kuhlmann <https://orcid.org/0000-0003-1783-3255>.

**Author contributions.** All authors contributed equally to analysing data and reaching conclusions, and in writing the paper.

## Appendix A. Kinetic and thermal energy budgets of the perturbation flow

Here, we present all terms entering the kinetic (2.27) and the thermal energy budget (2.28). The structures of the budgets for the liquid and gas phases are identical, i.e. formally the same terms arise. However, the budgets are obtained by integration over different volumes that the liquid and the gas occupy. In the following equations, the distinction between the liquid and gas phases is taken care of by using the integration volume  $V_i$  occupied by the liquid or the gas,  $i \in [l, g]$ , and by using the corresponding set of coefficients  $\alpha$  (see (2.7)). Furthermore, the integrals over the free surface carry different signs, where the lower sign applies to the gas phase.

The viscous and thermal energy dissipations can be expressed as

$$\mathcal{D}_{kin} = \frac{\alpha_v}{2} \int_{V_i} |\mathbf{S}'|^2 dV = \alpha_v \int_{V_i} (\nabla \times \mathbf{u}')^2 dV \pm 8\pi\alpha_v \int_{-1/2}^{1/2} (hh_{zz}\hat{w}^2 - \hat{v}^2) dz \quad (\text{A1a})$$

where  $\mathbf{S}' = \nabla \mathbf{u}' + (\nabla \mathbf{u}')^T$  and

$$\mathcal{D}_{th} = \frac{\alpha_\kappa}{Pr} \int_{V_i} (\nabla \vartheta')^2 dV, \quad (\text{A1b})$$

respectively. Since the neutral modes are determined only up to an arbitrary factor,  $\mathcal{D}_{kin}$  and  $\mathcal{D}_{th}$  are used to normalise all terms in the respective kinetic and thermal energy balances. This allows us to determine the relative importance of each term in the budget for the instability mechanism.

The normalised mechanical and thermal production terms in (2.27) and (2.28), respectively, are defined as

$$\sum_{j=1}^5 I_j = -\frac{Re}{\mathcal{D}_{kin}} \int_{V_i} \left( v'^2 \frac{u_0}{r} + u'^2 \frac{\partial u_0}{\partial r} + u'w' \frac{\partial u_0}{\partial z} + u'w' \frac{\partial w_0}{\partial r} + w'^2 \frac{\partial w_0}{\partial z} \right) dV, \quad (\text{A2a})$$

$$\sum_{j=1}^2 J_j = -\frac{Re}{\mathcal{D}_{th}} \int_{V_i} \vartheta' \left( u' \frac{\partial \vartheta_0}{\partial r} + w' \frac{\partial \vartheta_0}{\partial z} \right) dV, \quad (\text{A2b})$$

with  $j$  consecutively numbering the individual integrals  $I_j$  and  $J_j$  of the sums. The works done per unit time by thermocapillary forces acting at the liquid–gas interface are obtained as

$$M_r = \pm \frac{4\pi\alpha_v}{\mathcal{D}_{kin}} \int_{-1/2}^{1/2} h h_z \hat{u} \left( \frac{\partial \hat{w}}{\partial r} - \frac{\partial \hat{u}}{\partial z} \right) dz, \quad (\text{A3a})$$

$$M_\varphi = \pm \frac{4\pi\alpha_v}{\mathcal{D}_{kin}} \int_{-1/2}^{1/2} h \hat{v} \left( \frac{\partial \hat{v}}{\partial r} - \frac{\hat{v}^2}{h} - h_z \frac{\partial \hat{v}}{\partial z} \right) dz, \quad (\text{A3b})$$

$$M_z = \pm \frac{4\pi\alpha_v}{\mathcal{D}_{kin}} \int_{-1/2}^{1/2} h \hat{w} \left( \frac{\partial \hat{w}}{\partial r} + h_z \hat{w} - h_z \frac{\partial \hat{w}}{\partial z} \right) dz. \quad (\text{A3c})$$

The quantity

$$B = \frac{\alpha_\beta B d}{\mathcal{D}_{kin}} \int_{V_i} w' \vartheta' dV \quad (\text{A4})$$

represents the work done per unit time by buoyancy forces. Further, the heat transfer across the liquid–gas interface can be written as

$$H_{fs} = \pm \frac{2\pi\alpha_\kappa}{\mathcal{D}_{th} Pr} \int_{-1/2}^{1/2} h \left( \frac{\partial \hat{\vartheta}^2}{\partial r} - h_z \frac{\partial \hat{\vartheta}^2}{\partial z} \right) dz. \quad (\text{A5})$$

The sign of the rate of change of the total kinetic (and thermal) energy is related directly to the growth rate of the normal mode for which the energy budget is evaluated. Thus if one of the integral terms in (2.27) or (2.28) is positive (negative), then it contributes to a destabilisation (stabilisation) of the basic flow. Since each of the above integrands describes a particular local transport process, each term can be associated with a particular physical mechanism, either stabilising or destabilising the basic flow.

As in Nienhüser & Kuhlmann (2002), the normalised residuals of the kinetic and thermal energy budgets are defined as

$$\delta E_{kin} := \left| -\frac{dE_{kin}}{dt} - 1 + M_r + M_\varphi + M_z + \sum_{j=1}^5 I_j + B \right|, \quad (\text{A6a})$$

$$\delta E_{th} := \left| -\frac{dE_{th}}{dt} - 1 + \sum_{j=1}^2 J_j + H_{fs} \right|, \quad (\text{A6b})$$

respectively. They serve as an additional verification for the numerics. Since (2.27) and (2.28) must be satisfied exactly, the residuals must vanish. We typically find  $\delta E_{kin} < 0.03$  and  $\delta E_{th} < 0.01$ .

For the high Prandtl number  $Pr = 28$  investigated, we find the inertial terms to be always small with  $I_j < 0.05$ . Therefore, the velocity field of the basic flow does not enter practically the energy budget of the linear mode, and the work done by thermocapillary stresses  $M_r$ ,  $M_\varphi$  and  $M_z$  is almost perfectly balanced by the viscous dissipation. The basic velocity field merely serves to create a basic temperature field from which temperature perturbations can gain thermal energy via  $J_1$  and  $J_2$ .

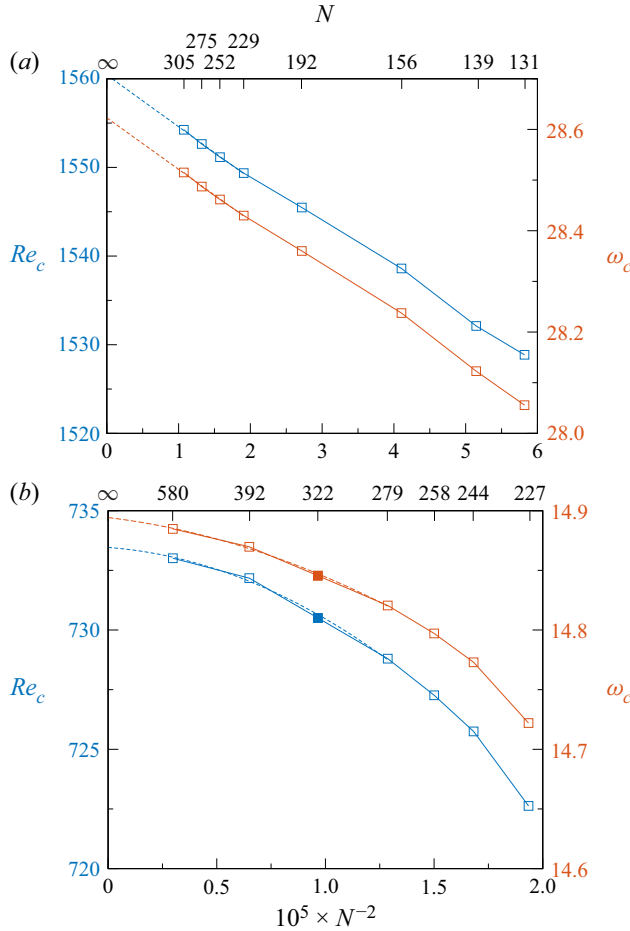


Figure 29. Critical data  $Re_c$  (blue symbols) and  $\omega_c$  (red symbols) as functions of the grid size  $N$  for the reference case with  $Pr = 28$ ,  $\Gamma_{ref} = 0.66$ ,  $\mathcal{V}_{ref} = 1$  and  $Bd_{ref} = 0.41$ . (a) Single-fluid model with adiabatic free surface, disregarding viscous stresses in the gas phase. The linear extrapolated critical data, using the four finest grids (dashed curves), are  $(Re_c, \omega_c)^{extra} = (1560, 28.62)$ . (b) Reference case (two-fluid model) including the gas phase. The critical data extrapolate quadratically (dashed curves) to  $(Re_c, \omega_c)^{extra} = (733.5, 14.89)$ . The solid symbols in (b) indicate the resolution used for production runs.

## Appendix B. Numerical tests

### B.1. Grid convergence

To prove grid convergence, we carry out a linear stability analysis for the reference case defined in § 2.5 – i.e. for  $Pr = 28$ ,  $\Gamma_{ref} = 0.66$ ,  $\mathcal{V}_{ref} = 1$  and  $Bd_{ref} = 0.41$  – and monitor the dependence of the critical Reynolds number  $Re_c$  and the critical frequency  $\omega_c = \text{Im}(\mu_c)$  as functions of  $N = \sqrt{N_{tot}}$ , where  $N_{tot}$  is the total number of finite volumes employed. For a second-order numerical scheme, the critical Reynolds number  $Re_c$  should scale  $\sim N^{-2}$  for large  $N$ . This behaviour is confirmed for the single-fluid model in which viscous stresses in the gas phase are neglected and the free surface is assumed to be adiabatic. The critical data for this simplified model ( $m_c = 4$ ) are shown in figure 29(a). It should be noted that the difference between  $Re_c(m = 4)$  and the closest neutral Reynolds number  $Re_n(m = 3)$  is less than 1 %. Linear regression of the data for the four



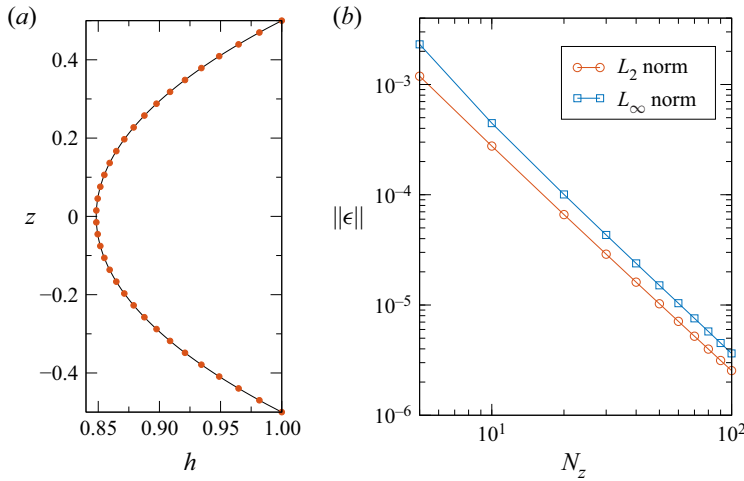


Figure 30. (a) Comparison of the catenoid profile  $h_{cat}(z)$  (line) according to (B1) with the numerical solution  $h(z)$  (red dots) of (3.1) for  $\Gamma = 1$  and  $h_0 = 0.848$  using an equidistant grid with  $N_z = 34$  grid points. (b)  $L_2$  and  $L_\infty$  norms of the deviation  $\epsilon$  of the numerical solution from the exact catenoid as functions of the number of grid points  $N_z$ .

finest grids (dashed lines in figure 29a) yields the extrapolated values  $(Re_c, \omega_c)^{extra} = (1560, 28.62)$ . These extrapolated values deviate by only (0.4 %, 0.4 %) from the critical data  $(Re_c, \omega_c)^{N=305} = (1554, 28.52)$  obtained on the finest mesh.

For the present two-fluid model that takes into account the gas phase, the critical wavenumber changes to  $m_c = 3$  and the Reynolds number is remarkably lower. The data do not show a linear convergence (figure 29b), because the grid is not homogeneous and involves grid points in the gas as well as in the liquid phase that are refined differently. Nevertheless, a regression with a polynomial of second order (dashed lines in figure 29b) yields  $(Re_c, \omega_c)^{extra} = (733.5, 14.89)$ . Since the finest mesh used in figure 29(b) is numerically too expensive for the intended quasi-continuous parameter variations, production runs were carried out using the resolution  $N = 322$  (solid symbols in figure 29b). The error is estimated by comparison of the extrapolated values  $(Re_c, \omega_c)^{extra}$  with the result  $(Re_c, \omega_c)^{N=322} = (730.5, 14.85)$ . Again, we arrive at an error estimate of at most 0.4 % for both the critical Reynolds number and the critical frequency. From these results, we conclude grid convergence and proceed using the grid  $N = 322$  for all stability analyses.

## B.2. Code verification

In a first verification step the interfacial shape is considered. In the case of weightlessness ( $Bo = 0$ ) the Young–Laplace equation (3.1) has the closed-form solution of a catenoid (Kenmotsu 1980; Langbein 2002):

$$h_{cat}(z) = h_0 \cosh\left(\frac{z}{h_0}\right), \quad (\text{B1})$$

where  $h_0 = h(0)$  is related to  $\Gamma$  by  $h_0 \cosh(1/2h_0) = 1/\Gamma$  (cf. (2.15)). In figure 30(a), we compare the numerically computed shape of the free surface with the catenoid profile for  $\Gamma = 1$  and  $h_0 = 0.848$ . The  $L_2$  and  $L_\infty$  norms of the deviation  $\epsilon = h(z) - h_{cat}(z)$  of the

Grid/ Reference	$Re = 3000$		$Re = 5000$		$Re = 7000$	
	$\tilde{\psi}_{max}$	$\log( \delta Nu )$	$\tilde{\psi}_{max}$	$\log( \delta Nu )$	$\tilde{\psi}_{max}$	$\log( \delta Nu )$
$121 \times 121$	2.1093	−12.3	2.0274	−12.2	1.9567	−12.4
$160 \times 160$	2.1171	−12.2	2.0306	−12.2	1.9622	−12.4
$260 \times 260$	2.1188	−13.1	2.0321	−12.9	1.9632	−12.5
$360 \times 360$	2.1193	−12.3	2.0324	−12.3	1.9634	−12.4
Leypoldt <i>et al.</i> (2000)	2.09	—	1.97	—	1.86	—
Nienhüser (2002)	—	—	2.03	−2.52	—	—
Romanò <i>et al.</i> (2017)	2.1783	—	2.0605	—	1.9735	—

Table 8. Scaled maximum absolute value of the Stokes stream function  $\tilde{\psi}_{max} = \max |\psi| \times 10^3$  and relative (logarithmic) error  $\delta Nu = \sum_i Nu_i / \max |Nu_i|$  of the total Nusselt number for the flow in a cylindrical liquid bridge with  $\Gamma = 1$ ,  $\mathcal{V} = 1$ ,  $Pr = 4$ ,  $Bd = 0$  and an adiabatic free surface for different grid resolutions. The comparison is made with Leypoldt *et al.* (2000), Nienhüser (2002) and Romanò *et al.* (2017).

numerical solution  $h(z)$  from the analytical counterpart  $h_{cat}(z)$  are displayed in figure 30(b) as functions of the number of grid points  $N_z$ , distributed uniformly over the height of the liquid bridge. From the graphs, a second-order convergence is obvious.

To verify the computations of the basic flow, the maximum absolute value of the Stokes stream function  $\psi$  arising in the centre of the thermocapillary vortex is compared with literature data of Leypoldt *et al.* (2000), Nienhüser (2002) and Romanò *et al.* (2017) for the single-fluid model. Data for different grids  $N_r \times N_z$  and Reynolds numbers are provided in table 8 for  $\Gamma = 1$ ,  $\mathcal{V} = 1$ ,  $Bd = 0$  and an adiabatic free surface. As can be seen, the present results are in good agreement with the literature data.

Apart from this local test, we checked the energy preservation by computing the total heat flux through the liquid bridge in non-dimensional form:

$$\sum_i Nu_i = - \sum_i \int_{S_i} \mathbf{n}_i \cdot \nabla \vartheta \, dS = 0, \quad (\text{B2})$$

where  $Nu_i$  is the Nusselt number for the circular hot and cold walls in contact with the liquid, and for the free surface ( $i \in [h, c, fs]$ ). Since the free surface is adiabatic,  $Nu_{fs} = 0$  and the heat flux through the cold wall must balance the heat flux through the hot wall. The relative error in the energy preservation of the basic state expressed by  $\delta Nu = \sum_i Nu_i / \max |Nu_i|$  is also provided in table 8. We find that the thermal energy of the basic state is conserved up to  $\delta Nu < 10^{-12}$  for all presented calculations. The same order of magnitude of  $\delta Nu$  was also obtained for cases with a non-vanishing heat flux through the free surface ( $Nu_{fs} \neq 0$ , not shown).

Finally, the linear stability analysis is verified by comparing with the critical parameters for the common benchmark of a cylindrical liquid bridge with  $\Gamma = 1$ ,  $Pr = 4$ ,  $Bd = 0$  and adiabatic free surface. Table 9 shows that our results for  $Re_c$  and  $\omega_c$ , and a resolution of  $N = 176 \times 197$  grid points in the radial and axial directions, respectively, deviate less than 0.2 % from the data of Levenstam *et al.* (2001) and Carrión *et al.* (2020). The deviation of  $Re_c$  by 0.8 % from the result of Levenstam *et al.* (2001) for  $Pr = 7$  is slightly larger. The somewhat larger deviation by 4.5 % of  $Re_c$  from the result of Wanschura *et al.* (1995) for  $Pr = 4$  can be explained by the regularisation of the thermocapillary stresses within 10 % of  $d$  from each corner employed by Wanschura *et al.* (1995). Since the regularisation tends to reduce the driving force, a higher critical Reynolds number was obtained by these authors. Furthermore, the deviation of  $Re_c$  by 2.8 % with respect to the result of Shevtsova,

Authors	Resolution	Pr = 4		Pr = 7	
		Re <sub>c</sub>	ω <sub>c</sub>	Re <sub>c</sub>	ω <sub>c</sub>
Present	176 × 197 (FV)	1002	28.43	876	22.91
Wanschura <i>et al.</i> (1995)	20 × 80 (Spectral, FD)	1047	27.9	—	—
Shevtsova <i>et al.</i> (2001)	(N <sub>r</sub> , N <sub>φ</sub> , N <sub>z</sub> ) = (25, 16, 21) (FV simulation)	1030	28.72	—	—
Levenstam <i>et al.</i> (2001)	41 × 41 (FE)	1002	28.5	869	22.9
Carrión <i>et al.</i> (2020)	91 × 91 (FD)	1000	28.45	—	—

Table 9. Critical data for common benchmarks ( $Pr = 4$  and  $7$ ) of a cylindrical liquid bridge with  $\Gamma = 1$ , adiabatic free surface, zero gravity, and negligible viscous stresses from the gas phase. A comparison is made with Wanschura *et al.* (1995), Shevtsova *et al.* (2001), Levenstam *et al.* (2001) and Carrión *et al.* (2020). Here, FV indicates finite volumes, FD indicates finite differences, and FE indicates finite elements.

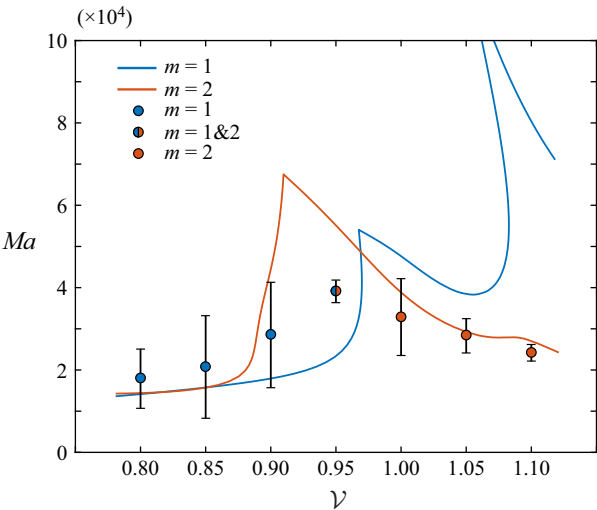


Figure 31. Neutral Marangoni numbers (lines) as function of the volume ratio  $\mathcal{V}$  for  $Pr = 28$ ,  $Bd = 0.92$ ,  $\Gamma = 1$ ,  $\Gamma_{rod} = 4.8$  and  $\eta = 5$ . A comparison is made with the experimental critical Marangoni numbers (symbols) extracted from figure 6(a) of Yano *et al.* (2016) for zero gas flow rate in the ambient air. The wavenumbers are  $m = 1$  (blue symbols) and  $m = 2$  (red symbols).

Melnikov & Legros (2001) could be related to their method of determining the critical onset by numerical simulation and by using a coarser mesh ( $25 \times 21$ ) in the  $(r, z)$  plane. In view of these comparisons, we consider our code verified.

### B.3. Code validation

For the purpose of validation, we also compared our linear stability analysis for  $Pr = 28$ ,  $\Gamma = 1$  and  $Bd = 0.92$  with the experimental data measured by Yano *et al.* (2016). To match with the experimental geometry, we adopted not only  $\Gamma$  and  $Bd$ , but also  $\eta = 5$  and  $\Gamma_{rod} = 4.8$ . Figure 31 shows the neutral and critical Marangoni numbers as functions of the volume ratio  $\mathcal{V}$ . As can be seen, the numerical critical Marangoni numbers, using resolution  $N = 322$ , agree with the experimental data within the experimental error bar.

Only for  $\mathcal{V} = 0.95$  does some deviation exist. This can be explained, however, by the nearby codimension-two points at which the azimuthal wavenumber of the critical mode changes from  $m = 1$  to  $m = 2$ . Near these points, the dynamics of the supercritical flow can be complicated. In fact, for  $\mathcal{V} = 0.95$ , Yano *et al.* (2016) found what they called a mixed mode with  $m = 1$  and  $m = 2$ , which must be a result of supercritical nonlinear interactions. Moreover, the critical curve for  $m = 1$  has a large slope with respect to  $\mathcal{V}$  such that small uncertainties in  $\mathcal{V}$  result in large deviations of the critical data. When comparing with the experiments, one has to keep in mind that the detailed experimental conditions may deviate to some degree from the numerical ones, and that the effect of temperature-dependent material parameters is not taken into account within the present modelling (except for  $\rho$ ,  $\rho_g$  and  $\sigma$ ). Given the remaining differences between experiment and numerics, and the relatively large error bar for the experimental critical Marangoni numbers measured by other authors, our code can also be considered validated.

#### REFERENCES

- BARMAK, I., ROMANÒ, F. & KUHLMANN, H.C. 2021 Finite-size coherent particle structures in high-Prandtl-number liquid bridges. *Phys. Rev. Fluids* **6**, 084301.
- BATCHELOR, G.K. & GILL, A.E. 1962 Analysis of the stability of axisymmetric jets. *J. Fluid Mech.* **14**, 529–551.
- CANRIGHT, D. 1994 Thermocapillary flow near a cold wall. *Phys. Fluids* **6**, 1415–1424.
- CARPENTER, B.M. & HOMSY, G.M. 1989 Combined buoyant–thermocapillary flow in a cavity. *J. Fluid Mech.* **207**, 121–132.
- CARRIÓN, L.M., HERRADA, M.A. & MONTANERO, J.M. 2020 Influence of the dynamical free surface deformation on the stability of thermal convection in high-Prandtl-number liquid bridges. *Intl J. Heat Mass Transfer* **146**, 118831.
- CHEN, Q.S. & HU, W.R. 1998 Influence of liquid bridge volume on instability of floating half zone convection. *Intl J. Heat Mass Transfer* **41**, 825–837.
- CHUN, C.H. & WUEST, W. 1979 Experiments on the transition from the steady to the oscillatory Marangoni-convection of a floating zone under reduced gravity effect. *Acta Astronaut.* **6** (9), 1073–1082.
- CRASTER, R.V. & MATAR, O.K. 2009 Dynamics and stability of thin liquid films. *Rev. Mod. Phys.* **81**, 1131–1198.
- CRÖLL, A., MÜLLER-SEBERT, W., BENZ, K.W. & NITSCHKE, R. 1991 Natural and thermocapillary convection in partially confined silicon melt zones. *Microgravity Sci. Technol.* **3**, 204–215.
- DIEZ, J.A. & KONDIC, L. 2002 Computing three-dimensional thin film flows including contact lines. *J. Comput. Phys.* **183** (1), 274–306.
- FU, B.-I. & OSTRACH, S. 1985 Numerical solution of thermocapillary flows in floating zones. In *Transport Phenomena in Materials Processing*, Power Engng Div. vol. 10, Heat Transfer Div. vol. 29, p. 1. ASME.
- FUJIMOTO, S., OGASAWARA, T., OTA, A., MOTEGI, K. & UENO, I. 2019 Effect of heat loss on hydrothermal wave instability in half-zone liquid bridges of high Prandtl-number fluid. *Intl J. Microgravity Sci. Appl.* **36**, 360204.
- FUJIMURA, K. 2013 Linear and weakly nonlinear stability of Marangoni convection in a liquid bridge. *J. Phys. Soc. Japan* **82**, 074401.
- GAPONENKO, Y., MIALDUN, V.Y.A., NEPOMNYASHCHY, A. & SHEVTSOVA, V. 2021 Hydrothermal waves in a liquid bridge subjected to a gas stream along the interface. *J. Fluid Mech.* **908**, A34.
- GAPONENKO, Y., MIALDUN, A. & SHEVTSOVA, V. 2012 Shear driven two-phase flows in vertical cylindrical duct. *Intl J. Multiphase Flow* **39**, 205–215.
- GOTTLIEB, R.G. & THOMPSON, B.F. 2010 Bisected direct quadratic *regula falsi*. *Appl. Maths Sci.* **4**, 709–718.
- HU, W.R., SHU, J.Z., ZHOU, R. & TANG, Z.M. 1994 Influence of liquid bridge volume on the onset of oscillation in floating zone convection. I. Experiments. *J. Crystal Growth* **142**, 379–384.
- HU, W.R., TANG, Z.M. & LI, K. 2008 Thermocapillary convection in floating zones. *Appl. Mech. Rev.* **61**, 010803.
- HURLE, D.T.J. & JAKEMAN, E. 1981 Introduction to the techniques of crystal growth. *PCH Phys. Chem. Hydrodyn.* **2** (4), 237–244.
- IMAISHI, N., YASUHIRO, S., AKIYAMA, Y. & YODA, S. 2001 Numerical simulation of oscillatory Marangoni flow in half-zone liquid bridge of low Prandtl number fluid. *J. Crystal Growth* **230**, 164–171.

- IRIKURA, M., ARAKAWA, Y., UENO, I. & KAWAMURA, H. 2005 Effect of ambient fluid flow upon onset of oscillatory thermocapillary convection in half-zone liquid bridge. *Microgravity Sci. Technol.* **16** (1), 176–180.
- KAMOTANI, Y. & OSTRACH, S. 1998 Theoretical analysis of thermocapillary flow in cylindrical columns of high Prandtl number fluids. *Trans. ASME J. Heat Transfer* **120**, 758–764.
- KAMOTANI, Y., WANG, L., HATTA, S., WANG, A. & YODA, S. 2003 Free surface heat loss effect on oscillatory thermocapillary flow in liquid bridges of high Prandtl number fluids. *Intl J. Heat Mass Transfer* **46**, 3211–3220.
- KANG, Q., WU, D., DUAN, L., HU, L., WANG, J., ZHANG, P. & HU, W. 2019 The effects of geometry and heating rate on thermocapillary convection in the liquid bridge. *J. Fluid Mech.* **881**, 951–982.
- KASPERSKI, G., BATOUL, A. & LABROSSE, G. 2000 Up to the unsteadiness of axisymmetric thermocapillary flows in a laterally heated liquid bridge. *Phys. Fluids* **12**, 103–119.
- KAWAMURA, H., NISHINO, K., MATSUMOTO, S. & UENO, I. 2012 Report on microgravity experiments of Marangoni convection aboard international space station. *Trans. ASME J. Heat Transfer* **134** (3), 031005.
- KAWAMURA, H. & UENO, I. 2006 Review on thermocapillary convection in a half-zone liquid bridge with high  $Pr$  fluid: onset of oscillatory convection, transition of flow regimes, and particle accumulation structure. In *Surface Tension-Driven Flows and Applications* (ed. R. Savino), chap. 1, pp. 1–24. Research Signpost.
- KENMOTSU, K. 1980 Surfaces of revolution with prescribed mean curvature. *Tôhoku Math. J.* **32** (1), 147–153.
- KUHLMANN, H.C. 1999 *Thermocapillary Convection in Models of Crystal Growth*. Springer Tracts in Modern Physics, vol. 152. Springer.
- KUHLMANN, H. & ALBENSOEDER, S. 2008 Three-dimensional flow instabilities in a thermocapillary-driven cavity. *Phys. Rev. E* **77**, 036303.
- KUHLMANN, H.C., LUKASSER, M. & MULDOON, F.H. 2011 Engineering Marangoni flows (EMA). ASAP6 819714. FFG.
- KUMAR, S. 2015 Liquid transfer in printing processes: liquid bridges with moving contact lines. *Annu. Rev. Fluid Mech.* **47**, 67–94.
- LANDAU, L.D. & LIFSHITZ, E.M. 1959 *Fluid Mechanics*. Pergamon Press.
- LANGBEIN, D. 2002 *Capillary surfaces: shape – stability – dynamics, in particular under weightlessness*. Springer Tracts in Modern Physics, vol. 178. Springer.
- LAPPA, M. 2003 Three-dimensional numerical simulation of Marangoni flow instabilities in floating zones laterally heated by an equatorial ring. *Phys. Fluids* **15**, 776–789.
- LAPPA, M. 2004 Combined effect of volume and gravity on the three-dimensional flow instability in noncylindrical floating zones heated by an equatorial ring. *Phys. Fluids* **16**, 331–343.
- LAPPA, M. 2005 Analysis of flow instabilities in convex and concave floating zones heated by an equatorial ring under microgravity conditions. *Comput. Fluids* **34**, 743–770.
- LAPPA, M., SAVINO, R. & MONTI, R. 2001 Three-dimensional numerical simulation of Marangoni instabilities in non-cylindrical liquid bridges in microgravity. *Intl J. Heat Mass Transfer* **44**, 1983–2003.
- LEHOUCQ, R.B., SORESENSEN, D.C. & YANG, C. 1998 *ARPACK Users' Guide: Solution of Large-Scale Eigenvalue Problems with Implicitly Restarted Arnoldi Methods*. SIAM.
- LEVENSTAM, M. & AMBERG, G. 1994 Hydrodynamical instabilities of thermocapillary flow in a half zone. Supplement of the PhD Thesis of M. Levenstam, KTH Stockholm.
- LEVENSTAM, M. & AMBERG, G. 1995 Hydrodynamic instabilities of thermocapillary flow in a half-zone. *J. Fluid Mech.* **297**, 357–372.
- LEVENSTAM, M., AMBERG, G. & WINKLER, C. 2001 Instabilities of thermocapillary convection in a half-zone at intermediate Prandtl numbers. *Phys. Fluids* **13**, 807–816.
- LEVICH, V.G. & KRYLOV, V.S. 1969 Surface tension-driven phenomena. *Annu. Rev. Fluid Mech.* **1**, 293–316.
- LEYPOLDT, J., KUHLMANN, H.C. & RATH, H.J. 2000 Three-dimensional numerical simulation of thermocapillary flows in cylindrical liquid bridges. *J. Fluid Mech.* **414**, 285–314.
- LEYPOLDT, J., KUHLMANN, H.C. & RATH, H.J. 2002 Stability of hydrothermal-wave states. *Adv. Space Res.* **29**, 645–650.
- LI, K., IMAISHI, N., JING, C.J. & YODA, S. 2007 Proper orthogonal decomposition of oscillatory Marangoni flow in half-zone liquid bridges of low- $Pr$  fluids. *J. Crystal Growth* **307** (1), 155–170.
- LI, K., MATSUMOTO, S., IMAISHI, N. & HU, W.-R. 2015 Marangoni flow in floating half zone of molten tin. *Intl J. Heat Mass Transfer* **83**, 575–585.
- LI, K., XUN, B., IMAISHI, N., YODA, S. & HU, W.R. 2008 Thermocapillary flows in liquid bridges of molten tin with small aspect ratios. *Intl J. Heat Fluid Flow* **29**, 1190–1196.
- MASUD, J., KAMOTANI, Y. & OSTRACH, S. 1997 Oscillatory thermocapillary flow in cylindrical columns of high Prandtl number fluids. *AIAA J. Thermophys. Heat Transfer* **11**, 105–111.



- MEERBERGEN, K., SPENCE, A. & ROOSE, D. 1994 Shift-invert and Cayley transforms for detection of eigenvalues with largest real part of nonsymmetric matrices. *BIT Numer. Maths* **34**, 409–423.
- MELNIKOV, D.E., SHEVTSOVA, V., YANO, T. & NISHINO, K. 2015 Modeling of the experiments on the Marangoni convection in liquid bridges in weightlessness for a wide range of aspect ratios. *Intl J. Heat Mass Transfer* **87**, 119–127.
- MIHALJAN, J.M. 1962 A rigorous exposition of the Boussinesq approximation applicable to a thin layer of fluid. *Astrophys. J.* **136**, 1126–1133.
- MILLS, K.C., KEENE, B.J., BROOKS, R.F. & SHIRALI, A. 1998 Marangoni effects in welding. *Phil. Trans. R. Soc. Lond. A* **356**, 911–925.
- MONTI, R., SAVINO, R. & LAPPÀ, M. 2000 Influence of geometrical aspect ratio on the oscillatory Marangoni convection in liquid bridges. *Acta Astronaut.* **47**, 753–761.
- MOTEGI, K., FUJIMURA, K. & UENO, I. 2017a Floquet analysis of spatially periodic thermocapillary convection in a low-Prandtl-number liquid bridge. *Phys. Fluids* **29** (7), 074104.
- MOTEGI, K., KUDO, M. & UENO, I. 2017b Linear stability of buoyant thermocapillary convection for a high-Prandtl number fluid in a laterally heated liquid bridge. *Phys. Fluids* **29** (4), 044106.
- NEITZEL, G.P., CHANG, K.-T., JANKOWSKI, D.F. & MITTELMANN, H.D. 1993 Linear-stability theory of thermocapillary convection in a model of the float-zone crystal-growth process. *Phys. Fluids A* **5**, 108–114.
- NIENHÜSER, C. 2002 Lineare Stabilität achsensymmetrischer thermokapillarer Konvektion in Flüssigkeitsbrücken mit statisch und dynamisch deformierbarer Grenzfläche. PhD thesis, Fachbereich Produktionstechnik. Universität Bremen.
- NIENHÜSER, C. & KUHLMANN, H.C. 2001 Dynamic free-surface deformations caused by steady axisymmetric and by time-dependent three-dimensional critical flows in thermocapillary half-zones. *Tech. Rep.* TMR-010015E. NASA.
- NIENHÜSER, C. & KUHLMANN, H.C. 2002 Stability of thermocapillary flows in non-cylindrical liquid bridges. *J. Fluid Mech.* **458**, 35–73.
- NIENHÜSER, C. & KUHLMANN, H.C. 2003 Corrigendum of *Stability of thermocapillary flows in non-cylindrical liquid bridges*, *J. Fluid Mech.* **458**, 35–73 (2002). *J. Fluid Mech.* **480**, 333–334.
- OHNISHI, M., AZUMA, H. & DOI, T. 1992 Computer simulation of oscillatory Marangoni flow. *Acta Astronaut.* **26**, 685–696.
- ORON, A., DAVIS, S.H. & BANKOFF, S.G. 1997 Long-scale evolution of thin liquid films. *Rev. Mod. Phys.* **69**, 931–980.
- PFANN, W.G. 1962 Zone melting. *Science* **135**, 1101–1109.
- PREISSER, F., SCHWABE, D. & SCHARMANN, A. 1983 Steady and oscillatory thermocapillary convection in liquid columns with free cylindrical surface. *J. Fluid Mech.* **126**, 545–567.
- ROMANÒ, F. & KUHLMANN, H.C. 2018 Finite-size Lagrangian coherent structures in thermocapillary liquid bridges. *Phys. Rev. Fluids* **3**, 094302.
- ROMANÒ, F. & KUHLMANN, H.C. 2019 Heat transfer across the free surface of a thermocapillary liquid bridge. *Tech. Mech.* **39**, 72–84.
- ROMANÒ, F., KUHLMANN, H.C., ISHIMURA, M. & UENO, I. 2017 Limit cycles for the motion of finite-size particles in axisymmetric thermocapillary flows in liquid bridges. *Phys. Fluids* **29** (9), 093303.
- ROMANÒ, F. & KUHLMANN, H.C. 2017 Particle–boundary interaction in a shear-driven cavity flow. *Theor. Comput. Fluid Dyn.* **31**, 427–445.
- SAKURAI, M., OHISHI, N. & HIRATA, A. 1996 Effect of liquid bridge form on oscillatory thermocapillary convection under normal gravity and microgravity conditions – drop shaft experiments. In *47th International Astronautical Congress*, paper number IAF–96–J.4.06. International Astronautical Federation.
- SAKURAI, M., OHISHI, N. & HIRATA, A. 2004 Effect of liquid bridge form on oscillatory thermocapillary convection under 1 g and  $\mu$ g conditions. *Acta Astronaut.* **55**, 977–983.
- SCHWABE, D. 1981 Marangoni effects in crystal growth melts. *Physicochem. Hydrodyn.* **2**, 263–280.
- SCHWABE, D. 2014 Thermocapillary liquid bridges and Marangoni convection under microgravity – results and lessons learned. *Microgravity Sci. Technol.* **26**, 1–10.
- SCHWABE, D., SCHARMANN, A., PREISSER, F. & OEDER, F. 1978 Experiments on surface tension driven flow in floating zone melting. *J. Crystal Growth* **43**, 305–312.
- SCRIVEN, L.E. & STERNLING, C.V. 1960 The Marangoni effects. *Nature* **187**, 186–188.
- SHEN, Y. 1989 Energy stability of thermocapillary convection in a model of float-zone crystal growth. PhD thesis, Arizona State University.
- SHEVTSOVA, V., GAPONENKO, Y., KUHLMANN, H.C., LAPPÀ, M., LUKASSER, M., MATSUMOTO, S., MIALDUN, A., MONTANERO, J.M., NISHINO, K. & UENO, I. 2014 The JEREMI-project on



- thermocapillary convection in liquid bridges. Part B: overview on impact of co-axial gas flow. *Fluid Dyn. Mater. Process.* **10**, 197–240.
- SHEVTSOVA, V., GAPONENKO, Y.A. & NEPOMNYASHCHY, A. 2013 Thermocapillary flow regimes and instability caused by a gas stream along the interface. *J. Fluid Mech.* **714**, 644–670.
- SHEVTSOVA, V.M. & LEGROS, J.C. 1998 Oscillatory convective motion in deformed liquid bridges. *Phys. Fluids* **10**, 1621–1634.
- SHEVTSOVA, V.M., MELNIKOV, D.E. & LEGROS, J.C. 2001 Three-dimensional simulations of hydrodynamic instability in liquid bridges: influence of temperature-dependent viscosity. *Phys. Fluids* **13**, 2851–2865.
- SHIN-ETSU 2004 *Silicone Fluid KF-96 – Performance Test Results*. 6-1, Ohtemachi 2-chome, Chioda-ku, Tokyo, Japan.
- SIM, B.C. & ZEBIB, A. 2002 Thermocapillary convection in liquid bridges with undeformable curved surfaces. *J. Thermophys. Heat Transfer* **16**, 553–561.
- SIMIC-STEFANI, S., KAWAJI, M. & YODA, S. 2006 Onset of oscillatory thermocapillary convection in acetone liquid bridges: the effect of evaporation. *Intl J. Heat Mass Transfer* **49**, 3167–3179.
- SIRIGNANO, W.A. & GLASSMAN, I. 1970 Flame spreading above liquid fuels: surface-tension-driven flows. *Combust. Sci. Technol.* **1**, 307–312.
- SLOBOZHANIN, L.A. & PERALES, J.M. 1993 Stability of liquid bridges between equal disks in an axial gravity field. *Phys. Fluids A* **5**, 1305–1314.
- SMITH, M.K. & DAVIS, S.H. 1983*a* Instabilities of dynamic thermocapillary liquid layers. Part 1. Convective instabilities. *J. Fluid Mech.* **132**, 119–144.
- SMITH, M.K. & DAVIS, S.H. 1983*b* Instabilities of dynamic thermocapillary liquid layers. Part 2. Surface-wave instabilities. *J. Fluid Mech.* **132**, 145–162.
- STOJANOVIC, M. & KUHLMANN, H.C. 2020*a* Flow instability in high-Prandtl-number thermocapillary liquid bridges exposed to a coaxial ambient gas stream. *Proc. Appl. Maths Mech.* **20**, e202000123.
- STOJANOVIC, M. & KUHLMANN, H.C. 2020*b* Stability of thermocapillary flow in high-Prandtl-number liquid bridges exposed to a coaxial gas stream. *Microgravity Sci. Technol.* **32**, 953–959.
- TAKAGI, K., OTAKA, M., NATSUI, H., ARAI, T., YODA, S., YUAN, Z., MUKAI, K., YASUHIRO, S. & IMAISHI, N. 2001 Experimental study on transition to oscillatory thermocapillary flow in a low Prandtl number liquid bridge. *J. Crystal Growth* **233**, 399–407.
- TANAKA, S., KAWAMURA, H., UENO, I. & SCHWABE, D. 2006 Flow structure and dynamic particle accumulation in thermocapillary convection in a liquid bridge. *Phys. Fluids* **18**, 067103.
- TANG, Z.M. & HU, W.R. 1999 Influence of liquid bridge volume on the onset of oscillation in floating half zone convection. III. Three-dimensional model. *J. Crystal Growth* **207**, 239–246.
- THEOFILIS, V. 2003 Advances in global linear instability analysis of nonparallel and three-dimensional flows. *Prog. Aerosp. Sci.* **39**, 249–315.
- THOMPSON, J.F., WARSI, Z.U. & MASTIN, C.W. 1985 *Numerical Grid Generation: Foundations and Applications*. Elsevier North-Holland.
- THOMSON, J. 1855 On certain curious motions observable at the surfaces of wine and other alcoholic liquors. *Lond. Edinb. Dublin Philos. Mag. J. Sci.* **10**, 330–333.
- UENO, I., KAWAZOE, A. & ENOMOTO, H. 2010 Effect of ambient-gas forced flow on oscillatory thermocapillary convection of half-zone liquid bridge. *Fluid Dyn. Mater. Process.* **6** (1), 99–108.
- UENO, I., TANAKA, S. & KAWAMURA, H. 2003 Oscillatory and chaotic thermocapillary convection in a half-zone liquid bridge. *Phys. Fluids* **15**, 408–416.
- UENO, I. & TORII, T. 2010 Thermocapillary-driven flow in a thin liquid film sustained in a rectangular hole with temperature gradient. *Acta Astronaut.* **66**, 1017–1021.
- VELTEN, R., SCHWABE, D. & SCHARMANN, A. 1991 The periodic instability of thermocapillary convection in cylindrical liquid bridges. *Phys. Fluids A* **3**, 267–279.
- WANSCHURA, M., KUHLMANN, H.C. & RATH, H.J. 1996 Three-dimensional instability of axisymmetric buoyant convection in cylinders heated from below. *J. Fluid Mech.* **326**, 399–415.
- WANSCHURA, M., KUHLMANN, H.C. & RATH, H.J. 1997*a* Instability of thermocapillary flow in symmetrically heated full liquid zones. In *Proceedings of the Joint Xth European and VIth Russian Symposium on Physical Science in Microgravity* (ed. V.S. Avduevsky & V.I. Polezhaev), vol. 1, pp. 172–173. St Petersburg.
- WANSCHURA, M., KUHLMANN, H.C. & RATH, H.J. 1997*b* Linear stability of two-dimensional combined buoyant-thermocapillary flow in cylindrical liquid bridges. *Phys. Rev. E* **55**, 7036–7042.
- WANSCHURA, M., SHEVTSOVA, V.S., KUHLMANN, H.C. & RATH, H.J. 1995 Convective instability mechanisms in thermocapillary liquid bridges. *Phys. Fluids* **7**, 912–925.

- WATANABE, T., MELNIKOV, D.E., MATSUGASE, T., SHEVTSOVA, V. & UENO, I. 2014 The stability of a thermocapillary-buoyant flow in a liquid bridge with heat transfer through the interface. *Microgravity Sci. Technol.* **26**, 17–28.
- WESSELING, P. 2009 *Principles of Computational Fluid Dynamics*. Springer.
- XU, J.-J. & DAVIS, S.H. 1984 Convective thermocapillary instabilities in liquid bridges. *Phys. Fluids* **27**, 1102–1107.
- XU, J. & ZEBIB, A. 1998 Oscillatory two- and three-dimensional thermocapillary convection. *J. Fluid Mech.* **364**, 187–209.
- XUN, B., LI, K. & HU, W.-R. 2010 Effect of volume ratio on thermocapillary flow in liquid bridges of high-Prandtl-number fluids. *Phys. Rev. E* **81**, 036324.
- YANO, T., HIROTANI, M. & NISHINO, K. 2018a Effect of interfacial heat transfer on basic flow and instability in a high-Prandtl-number thermocapillary liquid bridge. *Intl J. Heat Mass Transfer* **125**, 1121–1130.
- YANO, T., MARUYAMA, K., MATSUNAGA, T. & NISHINO, K. 2016 Effect of ambient gas flow on the instability of Marangoni convection in liquid bridges of various volume ratios. *Intl J. Heat Mass Transfer* **99**, 182–191.
- YANO, T., NISHINO, K., MATSUMOTO, S., UENO, I., KOMIYA, A., KAMOTANI, Y. & IMAISHI, N. 2018b Overview of ‘dynamic surf’ project in Kibo – dynamic behavior of large scale thermocapillary liquid bridges in microgravity. *Intl J. Microgravity Sci. Appl.* **35**, 350102.
- YANO, T., NISHINO, K., MATSUMOTO, S., UENO, I., KOMIYA, A., KAMOTANI, Y. & IMAISHI, N. 2018c Report on microgravity experiments of dynamic surface deformation effects on Marangoni instability in high-Prandtl-number liquid bridges. *Microgravity Sci. Technol.* **30**, 599–610.
- YANO, T., NISHINO, K., UENO, I., MATSUMOTO, S. & KAMOTANI, Y. 2017 Sensitivity of hydrothermal wave instability of Marangoni convection to the interfacial heat transfer in long liquid bridges of high Prandtl number fluids. *Phys. Fluids* **29** (4), 044105.
- YASNOU, V., GAPONENKO, Y., MIALDUN, A. & SHEVTSOVA, V. 2018 Influence of a coaxial gas flow on the evolution of oscillatory states in a liquid bridge. *Intl J. Heat Mass Transfer* **123**, 747–759.
- YOUNG, N.O., GOLDSTEIN, J.S. & BLOCK, M.J. 1959 The motion of bubbles in a vertical temperature gradient. *J. Fluid Mech.* **6**, 350–356.